

DTIC FILE COPY

4

GL-TR-89-0263

AD-A223 112

Atmospherically Induced Optical Contamination  
From Orbiting Thrusters

J. B. Elgin  
M. Tautz

Spectral Sciences, Inc  
99 South Bedford Street  
Burlington, MA 01803-5169

19 September 1989

Scientific Report No. 1

APPROVED FOR PUBLIC RELEASE; DISTRIBUTION UNLIMITED


GEOPHYSICS LABORATORY  
AIR FORCE SYSTEMS COMMAND  
UNITED STATES AIR FORCE  
HANSCOM AIR FORCE BASE, MASSACHUSETTS 01731-5000

DTIC  
ELECTE  
JUN 13 1990  
S B D  
cc

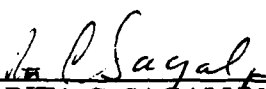
90 36 12 140

"This technical report has been reviewed and is approved for publication"

  
EDMOND MURAD  
Contract Manager

  
CHARLES P. PIKE, Chief  
Spacecraft Interactions Branch

FOR THE COMMANDER

  
RITA C. SAGALYN, Director  
Space Physics Division

This report has been reviewed by the ESD Public Affairs Office (PA) and is releasable to the National Technical Information Service (NTIS)

Qualified requestors may obtain additional copies from the Defense Technical Information Center. All others should apply to the National Technical Information Service.

If your address has changed, or if you wish to be removed from the mailing list, or if the addressee is no longer employed by your organization, please notify GL/IMA, Hanscom AFB, MA, 01731. This will assist us in maintaining a current mailing list.

Do not return copies of this report unless contractual obligations or notices on a specific document requires that it be returned.

**UNCLASSIFIED**

SECURITY CLASSIFICATION OF THIS PAGE

**REPORT DOCUMENTATION PAGE**

1. REPORT SECURITY CLASSIFICATION UNCLASSIFIED			1b. RESTRICTIVE MARKINGS			
2a. SECURITY CLASSIFICATION AUTHORITY N/A			3. DISTRIBUTION/AVAILABILITY OF REPORT Approved for public release; distribution unlimited			
3. DECLASSIFICATION/DOWNGRADING SCHEDULE N/A			5. MONITORING ORGANIZATION REPORT NUMBER(S) GL-TR-89-0263			
4. PERFORMING ORGANIZATION REPORT NUMBER(S) SSI-TR-160			7a. NAME OF MONITORING ORGANIZATION Geophysics Laboratory			
5a. NAME OF PERFORMING ORGANIZATION Spectral Sciences, Inc.		6b. OFFICE SYMBOL (If applicable) N/A		7b. ADDRESS (City, State, and ZIP Code) Hanscom AFB, MA 01731-5000		
7. ADDRESS (City, State, and ZIP Code) 99 South Bedford Street Burlington, MA 01803-5169		8a. NAME OF FUNDING/SPONSORING ORGANIZATION Geophysics Laboratory		9. PROCUREMENT INSTRUMENT IDENTIFICATION NUMBER F19628-88-C-0074		
8b. ADDRESS (City, State, and ZIP Code) Hanscom AFB, MA 01731		8b. OFFICE SYMBOL (If applicable) OPB		10. SOURCE OF FUNDING NUMBERS		
				PROGRAM ELEMENT NO. 62101F	PROJECT NO. 7601	
				TASK NO. 30	WORK UNIT ACCESSION NO. BB	
11. TITLE (Include Security Classification) Atmospherically Induced Optical Contamination from Orbiting Thrusters						
12. PERSONAL AUTHOR(S) J. B. Elgin and M. Tautz <sup>@</sup>						
13a. TYPE OF REPORT Scientific NO. 1		13b. TIME COVERED FROM 09MAY88 TO 31AUG89		14. DATE OF REPORT (Year, Month, Day) 19 September 1989		
				15. PAGE COUNT 66		
16. SUPPLEMENTARY NOTATION Radex, Inc. Bedford, MA 01730						
17. COSATI CODES			18. SUBJECT TERMS (Continue on reverse if necessary and identify by block number)			
FIELD	GROUP	SUB-GROUP				
			contamination radiation space shuttle			
19. ABSTRACT (Continue on reverse if necessary and identify by block number)  We present in this paper, results of the SOCRATES (Shuttle Orbiter Contamination Representation Accounting for Transiently Emitted Species) code which has been developed to assess the effects of contamination on measurements aboard spacecraft in low earth orbit. SOCRATES is a Monte Carlo code which includes in its present version scattering, collisions leading to kinetic-to-vibrational energy transfer, and reactive collisions. The application of this code to actual measurements aboard spacecraft in low earth orbit makes it possible to evaluate data obtained on these platforms with a view towards extracting the data of interest from contaminated signals.						
20. DISTRIBUTION/AVAILABILITY OF ABSTRACT <input type="checkbox"/> UNCLASSIFIED/UNLIMITED <input checked="" type="checkbox"/> SAME AS RPT. <input type="checkbox"/> DTIC USERS			21. ABSTRACT SECURITY CLASSIFICATION UNCLASSIFIED			
22a. NAME OF RESPONSIBLE INDIVIDUAL Edmund Murad			22b. TELEPHONE (Include Area Code)		22c. OFFICE SYMBOL GL/PHK	

**UNCLASSIFIED**

## TABLE OF CONTENTS

<u>Section</u>	<u>Page</u>
1 INTRODUCTION . . . . .	1
1.1 Overview . . . . .	1
1.2 Methodology . . . . .	2
2 CASE DEFINITIONS . . . . .	5
2.1 Physical Parameters . . . . .	5
2.2 Coordinate System . . . . .	5
2.3 Far Field Line-Of-Sight Integrations . . . . .	6
2.3 Near Field Line-Of-Sight Integrations . . . . .	6
3 SCATTERING RESULTS . . . . .	9
4 T-V COLLISIONS . . . . .	23
5 REACTIVE COLLISIONS . . . . .	33
6 SUMMARY . . . . .	57



<b>Accession For</b>	
NTIS GRA&I	<input checked="" type="checkbox"/>
DTIC TAB	<input type="checkbox"/>
Unannounced	<input type="checkbox"/>
Justification _____	
By _____	
Distribution/	
Availability Codes	
Dist	Avail and/or Special
A-1	

## LIST OF FIGURES

<u>Figure</u>		<u>Page</u>
1	An arbitrary viewing direction represented by a unit vector, $\hat{i}_v$ , within the SOCRATES cartesian coordinate system . . . . .	8
2	A panel of gray scale plots showing the $H_2O$ column density resulting from VRCS firings at 200, 400, and 600 Km, each at three angles of attack: 0, 90, and $180^\circ$ . . . . .	10
3	A panel of contour plots showing the $H_2O$ column density resulting from VRCS firings at 200, 400, and 600 Km, each at three angles of attack: 0, 90, and $180^\circ$ . . . . .	11
4	A panel of gray scale plots showing the $H_2O$ column density resulting from VRCS firings at 200, 400, and 600 Km, each at three angles of attack: 0, 90, and $180^\circ$ . . . . .	12
5	A panel of contour plots showing the $H_2O$ column density resulting from VRCS firings at 200, 400, and 600 Km, each at three angles of attack: 0, 90, and $180^\circ$ . . . . .	13
6	A panel of gray scale plots showing the $CO_2$ column density resulting from VRCS firings at 200, 400, and 600 Km, each at three angles of attack: 0, 90, and $180^\circ$ . . . . .	14
7	A panel of contour plots showing the $CO_2$ column density resulting from VRCS firings at 200, 400, and 600 Km, each at three angles of attack: 0, 90, and $180^\circ$ . . . . .	15
8	A panel of gray scale plots showing the $CO_2$ column density resulting from VRCS firings at 200, 400, and 600 Km, each at three angles of attack: 0, 90, and $180^\circ$ . . . . .	16
9	A panel of contour plots showing the $CO_2$ column density resulting from VRCS firings at 200, 400, and 600 Km, each at three angles of attack: 0, 90, and $180^\circ$ . . . . .	17
10	A panel of gray scale plots showing the $H_2$ column density resulting from VRCS firings at 200, 400, and 600 Km, each at three angles of attack: 0, 90, and $180^\circ$ . . . . .	18
11	A panel of contour plots showing the $H_2$ column density resulting from VRCS firings at 200, 400, and 600 Km, each at three angles of attack: 0, 90, and $180^\circ$ . . . . .	19

# LIST OF FIGURES (Cont.)

<u>Figure</u>		<u>Page</u>
12	A panel of gray scale plots showing the $H_2$ column density resulting from VRCS firings at 200, 400, and 600 Km, each at three angles of attack: 0, 90, and $180^\circ$ . . . . .	20
13	A panel of contour plots showing the $H_2$ column density resulting from VRCS firings at 200, 400, and 600 Km, each at three angles of attack: 0, 90, and $180^\circ$ . . . . .	21
14	A comparison of the $H_2$ and $H_2O$ number densities at an altitude of 200 Km and $0^\circ$ angle of attack for a position 2.1 km downstream from the exit plane . . . . .	22
15	A panel of gray scale plots showing the $H_2O$ $v_3$ emission at $2.7 \mu m$ due to excitation from collisions with atomic oxygen . . . . .	24
16	A panel of contour plots showing the $H_2O$ $v_3$ emission at $2.7 \mu m$ due to excitation from collisions with atomic oxygen . . . . .	25
17	A panel of gray scale plots showing the $H_2O$ $v_3$ emission at $2.7 \mu m$ due to excitation from collisions with atomic oxygen . . . . .	26
18	A panel of contour plots showing the $H_2O$ $v_3$ emission at $2.7 \mu m$ due to excitation from collisions with atomic oxygen . . . . .	27
19	A panel of gray scale plots showing the $CO_2$ $v_3$ emission at $4.3 \mu m$ due to excitation from collisions with atomic oxygen . . . . .	28
20	A panel of contour plots showing the $CO_2$ $v_3$ emission at $4.3 \mu m$ due to excitation from collisions with atomic oxygen . . . . .	29
21	A panel of gray scale plots showing the $CO_2$ $v_3$ emission at $4.3 \mu m$ due to excitation from collisions with atomic oxygen . . . . .	30
22	A panel of contour plots showing the $CO_2$ $v_3$ emission at $4.3 \mu m$ due to excitation from collisions with atomic oxygen . . . . .	31

# LIST OF FIGURES (Cont.)

<u>Figure</u>		<u>Page</u>
23	A panel of gray scale plots showing the OH vibrational emission at 2.7 $\mu\text{m}$ as a result of the reaction of $\text{O} + \text{H}_2\text{O} \rightarrow \text{OH}^* + \text{OH}$ . . . . .	35
24	A panel of contour plots showing the OH vibrational emission at 2.7 $\mu\text{m}$ as a result of the reaction of $\text{O} + \text{H}_2\text{O} \rightarrow \text{OH}^* + \text{OH}$ . . . . .	36
25	A panel of gray scale plots showing the OH vibrational emission at 2.7 $\mu\text{m}$ as a result of the reaction of $\text{O} + \text{H}_2\text{O} \rightarrow \text{OH}^* + \text{OH}$ . . . . .	37
26	A panel of contour plots showing the OH vibrational emission at 2.7 $\mu\text{m}$ as a result of the reaction of $\text{O} + \text{H}_2\text{O} \rightarrow \text{OH}^* + \text{OH}$ . . . . .	38
27	A panel of gray scale plots showing the OH vibrational emission at 2.7 $\mu\text{m}$ as a result of the reaction of $\text{O} + \text{H}_2 \rightarrow \text{OH}^* + \text{H}$ . . . . .	39
28	A panel of contour plots showing the OH vibrational emission at 2.7 $\mu\text{m}$ as a result of the reaction of $\text{O} + \text{H}_2 \rightarrow \text{OH}^* + \text{H}$ . . . . .	40
29	A panel of gray scale plots showing the OH vibrational emission at 2.7 $\mu\text{m}$ as a result of the reaction of $\text{O} + \text{H}_2 \rightarrow \text{OH}^* + \text{H}$ . . . . .	41
30	A panel of contour plots showing the OH vibrational emission at 2.7 $\mu\text{m}$ as a result of the reaction of $\text{O} + \text{H}_2 \rightarrow \text{OH}^* + \text{H}$ . . . . .	42
31	A comparison of OH vibrational emission at 2.7 $\mu$ for the mechanisms of $\text{O} + \text{H}_2\text{O}$ and $\text{O} + \text{H}_2$ . . . . .	43
32	A panel of gray scale plots showing the total OH vibrational emission at 2.7 $\mu\text{m}$ as a result of the reactions $\text{O} + \text{H}_2\text{O} \rightarrow \text{OH}^* + \text{OH}$ and $\text{O} + \text{H}_2 \rightarrow \text{OH}^* + \text{H}$ . . . . .	44
33	A panel of contour plots showing the total OH vibrational emission at 2.7 $\mu\text{m}$ as a result of the reactions $\text{O} + \text{H}_2\text{O} \rightarrow \text{OH}^* + \text{OH}$ and $\text{O} + \text{H}_2 \rightarrow \text{OH}^* + \text{H}$ . . . . .	45
34	A panel of gray scale plots showing the total OH vibrational emission at 2.7 $\mu\text{m}$ as a result of the reactions $\text{O} + \text{H}_2\text{O} \rightarrow \text{OH}^* + \text{OH}$ and $\text{O} + \text{H}_2 \rightarrow \text{OH}^* + \text{H}$ . . . . .	46

# LIST OF FIGURES (Cont.)

<u>Figure</u>		<u>Page</u>
35	A panel of contour plots showing the total OH vibrational emission at 2.7 $\mu\text{m}$ as a result of the reactions $\text{O} + \text{H}_2\text{O} \rightarrow \text{OH}^* + \text{OH}$ and $\text{O} + \text{H}_2 \rightarrow \text{OH}^* + \text{H}$ . . . . .	47
36	A panel of gray scale plots showing the OH ultraviolet emission at 306.4 nm as a result of the reaction $\text{O} + \text{H}_2\text{O} \rightarrow \text{OH(A)} + \text{OH}$ . . . . .	49
37	A panel of contour plots showing the OH ultraviolet emission at 306.4 nm as a result of the reaction $\text{O} + \text{H}_2\text{O} \rightarrow \text{OH(A)} + \text{OH}$ . . . . .	50
38	A panel of gray scale plots showing the OH ultraviolet emission at 306.4 nm as a result of the reaction $\text{O} + \text{H}_2\text{O} \rightarrow \text{OH(A)} + \text{OH}$ . . . . .	51
39	A panel of contour plots showing the OH ultraviolet emission at 306.4 nm as a result of the reaction $\text{O} + \text{H}_2\text{O} \rightarrow \text{OH(A)} + \text{OH}$ . . . . .	52
40	A panel of gray scale plots showing the CO vibrational emission at 4.6 $\mu\text{m}$ as a result of the reaction of $\text{O} + \text{CO}_2 \rightarrow \text{CO}^* + \text{O}_2$ . . . . .	53
41	A panel of contour plots showing the CO vibrational emission at 4.6 $\mu\text{m}$ as a result of the reaction of $\text{O} + \text{CO}_2 \rightarrow \text{CO}^* + \text{O}_2$ . . . . .	54
42	A panel of gray scale plots showing the CO vibrational emission at 4.6 $\mu\text{m}$ as a result of the reaction of $\text{O} + \text{CO}_2 \rightarrow \text{CO}^* + \text{O}_2$ . . . . .	55
43	A panel of contour plots showing the CO vibrational emission at 4.6 $\mu\text{m}$ as a result of the reaction of $\text{O} + \text{CO}_2 \rightarrow \text{CO}^* + \text{O}_2$ . . . . .	56



## LIST OF TABLES

<u>Table</u>		<u>Page</u>
1	Shuttle Engine Combustion Products . . . . .	7
2	Composition of the Low-Earth Orbit Atmosphere . . . . .	7
3	Total Solution Region Emission (Watts/Sr) . . . . .	32
4	Rate Coefficients Used in SOCRATES . . . . .	48

## 1. INTRODUCTION

### 1.1 OVERVIEW

The ability to conduct long term experiments in space has necessitated understanding the local environment of the measuring platform in order to be able to sort out the perturbations generated by the measuring platform on the phenomena being measured. A number of attempts have been made to model, in a piecemeal fashion, the effect of contamination on sensors flown on the Space Shuttle. Many of the earlier attempts have treated contamination as being due solely, or primarily, to the exhaust products of thruster motors.<sup>(1-3)</sup> Of course, spacecraft contamination is indeed related to the flow fields of the exhaust products of spacecraft engines, as has been demonstrated in a Monte Carlo code developed for that specific purpose of understanding the backflow of exhaust products into the shuttle bay.<sup>(4)</sup> This report describes calculations performed with SOCRATES (Spacecraft/Orbiter Contamination Representation Accounting for Transiently Emitted Species) which has been developed with the idea of addressing in a comprehensive manner the problem of contamination on spacecraft. SOCRATES builds on a plume code developed for a different application<sup>(5)</sup> and tries to assess the flow fields of contaminants in the low earth orbit environment taking into account not only scattering but reactive collisions. The importance of this effort arises from the fact that at orbital velocity in low earth orbit ( $7.7 \text{ km s}^{-1}$ ) spacecraft surfaces as well as the gaseous envelope of the spacecraft are constantly bombarded by atomic oxygen. The velocity distribution of the O atoms is typical of ionospheric temperature, measured as  $750 \pm 50 \text{ K}$  on one occasion.<sup>(6)</sup> At orbital velocity the energy of O is 4.9 eV, so the potential for undergoing endothermic reactions is great. The timeliness of code development is particularly propitious because of the availability of data from some Space Shuttle flights where diagnostic instruments, e.g. mass spectrometers<sup>(7-13)</sup> and plasma diagnostics<sup>(14)</sup> were flown. It has been clearly shown in these experiments that gases from some of the exhaust jets are reflected into the

exhaust jets are reflected into the bay of the Space Shuttle, the amount being dependent on the orientation of the VRCS with respect to the velocity vector and with respect to the shuttle surfaces. (10,13)

The eventual aim in the development of SOCRATES is the inclusion of gas phase neutral-neutral reactions, neutral-surface reactions, and neutral-ion reactions and to validate the code against the measurements reported above as well as against those which measured surface interactions. (15) This report presents calculations performed with the first module of SOCRATES, which is the Monte Carlo module for far field neutral gas interactions.

## 1.2 METHODOLOGY

The direct simulation Monte Carlo method involves storing a discrete number of molecules (via their velocities, positions, and other pertinent information) in a computer. The solution region is broken up into a number of separate cells, and the solution is stepped forward in time in a two stage process. First, the molecules are advanced along their trajectories by an amount appropriate to their velocity and a time increment,  $\Delta t_m$ . In this first stage some molecules will leave the solution region, and some will be introduced as determined by the boundary conditions for a particular problem. The second stage is to simulate collisions in each cell appropriate to  $\Delta t_m$  so that collision frequencies are properly simulated. A basic hypothesis of the method is that if the time step is made small enough, the processes of translations and collisions can be uncoupled in this manner.

Periodically, the solution is sampled by accumulating statistical sums of number densities, velocities and other basic properties. The solution is run repeatedly until statistical deviations are reduced to a desired limit, and then physically meaningful output quantities are computed from the statistical sums. The number of molecules represented is typically many thousand at a time, which is vastly fewer than the number occurring in virtually all real flows. Hence, the construction of a dynamically similar flow to be simulated in the computer is an essential feature of the method.

In order to successfully apply this technique to the contamination flow fields of interest, consideration must be given to the basic character of these flows. A molecule leaving the shuttle can be expected to experience its first collision with an atmospheric species at a distance,  $\lambda_c$ , from the shuttle which depends on the local conditions. Typically, for unperturbed space,  $\lambda_c$  may be on the order of a few hundred meters at an altitude of 200 km, some tens of kilometers at 400 km, and hundreds of kilometers at an altitude of 600 km. The solution region must extend to several  $\lambda_c$  if the scattering process is to be accurately represented, which is necessary for calculating atmospheric backscatter or radiative emission resulting from these collisions.

A fundamental problem arises in describing accurately the interaction of the scattered flow with the shuttle as  $\lambda_c$  becomes large, since cell sizes must be small compared to shuttle dimensions. The required number of cells for such a complete solution makes the complete calculation intractable. However, advantage can be taken of the separation of length scales to achieve the same result with much less computational effort. This is done by separating the solution into an "inner" and an "outer" solution, the latter being performed first.

The outer solution is performed on a length scale of the interaction of the contaminants with the atmosphere, i.e., several  $\lambda_c$ . On this length scale the dimensions of the shuttle are unimportant, and the sources of contaminants are treated as emanating from the origin. There are no shuttle surfaces considered in the outer solution, and the smallest cells are large with respect to shuttle dimensions. The outer solution is generated by the first module of SOCRATES, which is described in this paper.

The inner solution is performed by the second module of SOCRATES, which is still under development. The inner solution comprises the immediate shuttle vicinity, and takes as a boundary condition the results from the outer solution for the inwardly directed fluxes of the species in the simulation. The inner solution handles the detailed interaction of the contaminant cloud with the shuttle vehicle, as well as direct contamination from sources such as the backflow from a thruster. In the inner solution, all sources are properly located on the vehicle.

Once the inner and outer solution have been finished, then ion-neutral interactions will be included in the code. This modification will require a number of detailed kinetic data as well as inclusion of electric fields into the model.

## 2. CASE DEFINITIONS

### 2.1 PHYSICAL PARAMETERS

Calculations have been performed for the interaction between the ambient atmosphere and the steady state exhaust from a Space Shuttle VRCS (Vernier Reaction Control System) engine. It should be stressed that this choice is arbitrary and is not a limit of SOCRATES. A suite of nine calculations were performed, for altitudes of 200, 400, and 600 km, and angles of attack between the oncoming wind and the centerline exhaust direction of 0, 90, and 180 degrees. (A 180° angle of attack corresponds to firing the VRCS in the upwind direction, while 0° corresponds to the downwind direction.)

The predicted composition of the exhaust is shown in Table 1 and is based on thermodynamic equilibrium at 3000 K (quoted by Pickett et al.<sup>(9)</sup>). The constituents of the exhaust interact with the ambient atmosphere, whose composition is given in Table 2.

The VRCS engines release gases at a velocity which is typical of chemical rockets, about 3 km/s. Hence, the relative velocity between exhaust and atmospheric species varies from about 4.7 to 10.7 km/s, depending on the angle between the exhaust and atmospheric velocity vectors. For atomic oxygen colliding with water, for example, this corresponds to an energy range of about 1 to 5 eV. Therefore, a substantial range of collision energies is available depending on the relative velocity between the exhaust and atmospheric species.

### 2.2 COORDINATE SYSTEM

A Cartesian coordinate system was used with its origin at the shuttle and the +X direction fixed as the direction of shuttle motion. This means that for an observer fixed with respect to the shuttle, the atmospheric wind is heading in the -X direction. For the 0° angle of attack cases the centerline exhaust direction is also in the -X direction, while it was

taken to be in the +Z direction for  $90^\circ$  and +X direction for  $180^\circ$  angles of attack. Hence, the X-Z plane is a symmetry plane for all cases, while the  $0^\circ$  and  $180^\circ$  cases are also axially symmetric with respect to the X axis.

### 2.3 FAR FIELD LINE-OF-SIGHT INTEGRATIONS

As was discussed in Section 1, the scale lengths for the interactions were substantially different in many of the cases, making a common spatial scale impractical. Hence, when comparing results at different altitudes, the reader should remember that the presentation length scales may be quite different. In many cases the results are presented as integrated along the Y direction, which shows how they would appear to a distant observer. This is mainly done in order to reduce the dimensionality of the presentation, while retaining substantial physical meaning. The presentation of quantities which vary as a function of three spatial dimensions is not straightforward on two dimensional paper.

The far field integrations are presented in two forms: gray scale and contour plots. The gray scale plots have the advantage that they give an immediate visual impression of the relative magnitude of the spatial variation of a quantity. The contour plots have the advantage that they can be more quantitatively read.

### 2.4 NEAR FIELD LINE-OF-SIGHT INTEGRATIONS

Finally, an attempt was made to calculate the quantities as they would be seen by an observer located within the shuttle bay as a function of look angle. Such calculations can only be done accurately after the inner solution portion of SOCRATES is complete, at which time substantially more detail would be expected.

When a particular viewing direction is considered from the shuttle, it is represented by the angles  $\alpha$  and  $\beta$ . These angles are illustrated in Figure 1, which shows an arbitrary viewing direction represented by the viewing direction unit vector  $\vec{I}_v$ .  $\alpha$  is the angle between the +X direction and  $\vec{I}_v$ , and  $\beta$  is the angle between the +Y direction and the projection of  $\vec{I}_v$  into the Y-Z plane. Hence,  $\vec{I}_v$  is represented in terms of  $\alpha$  and  $\beta$  as

$$\vec{I}_V = \cos(\alpha)\vec{I}_X + \sin(\alpha)\cos(\beta)\vec{I}_Y + \sin(\alpha)\sin(\beta)\vec{I}_Z \quad (1)$$

This definition was chosen since for the axisymmetric cases there is no  $\beta$  dependence for quantities integrated along a line of sight. The near field results will also be shown for both gray scale and contour plots.

TABLE 1  
Shuttle Engine Combustion Products\*

Species	Mole Fraction	Molecular Weight (AMU)
H <sub>2</sub> O	0.33	18
N <sub>2</sub>	0.31	28
H <sub>2</sub>	0.16	2
CO	0.13	28
CO <sub>2</sub>	0.042	44
O <sub>2</sub>	0.002	32
NO	0.001	30
OH	Trace	17
N <sub>2</sub> O	Trace	44

\* Calculated composition assuming thermodynamic equilibrium at the combustion temperature. Results given in NASA Handbook and quoted by Pickett et al.<sup>(9)</sup>

TABLE 2  
Composition of the Low-Earth Orbit Atmosphere<sup>(16)</sup>  
(Molecules/cm<sup>3</sup>)

Species	Altitude (km)		
	200	400	600
H			1.1x10 <sup>5</sup>
O	4.6x10 <sup>9</sup>	4.8x10 <sup>7</sup>	8.3x10 <sup>5</sup>
N <sub>2</sub>	1.7x10 <sup>9</sup>	6.2x10 <sup>5</sup>	5x10 <sup>2</sup>
O <sub>2</sub>	1.2x10 <sup>8</sup>	1.5x10 <sup>5</sup>	4.4



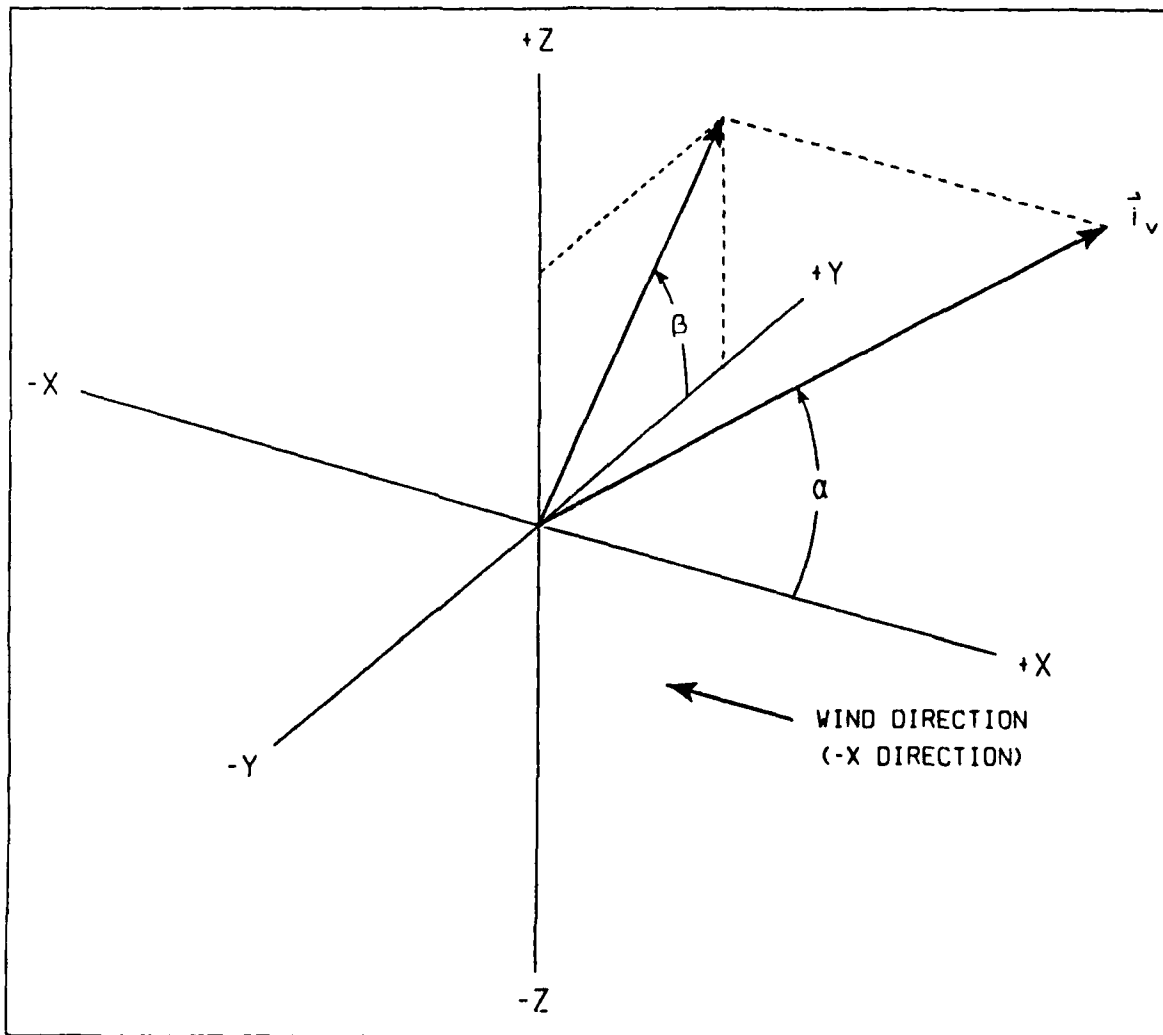


Figure 1. An arbitrary viewing direction represented by a unit vector,  $\vec{i}_v$ , within the SOCRATES cartesian coordinate system.  $\alpha$  is the angle between the +X direction and  $\vec{i}_v$ , and  $\beta$  is the angle between the +Y direction and the projection of  $\vec{i}_v$  into the Y-Z plane.

### 3. SCATTERING RESULTS

Figures 2-5 contain panels of the  $H_2O$  column density for the nine calculations. Figures 2 and 3 show the column densities obtained by integrating along the Y direction, in gray scale and contour form, respectively. Figures 4 and 5 show the column densities obtained by integrating along various directions from the shuttle bay, as a function of the look angles  $\alpha$  and  $\beta$  defined in the previous section. These figures make it clear that the choice for the look angles provides results which are independent of  $\beta$  for the axisymmetric cases. In the spatial plots (Figures 2 and 3), the atmospheric wind is approaching from the right. The three left panels show the altitude variation for aligned ( $0^\circ$ ) plumes. The effect of the atmospheric wind increasingly confining the plume as the altitude is decreased can be seen clearly in the Figures, even with the varying length scales. For the  $90^\circ$  angle of attack cases (the center columns) the plume is blown back substantially within the first kilometer at 200 km altitude, but it takes about ten kilometers for substantial turning to be evident at 400 km. At 600 km the plume seems largely unaffected by the atmosphere. Qualitatively similar results are evident for the retrofire ( $180^\circ$ ) cases shown in the right column. Figures 6-9 and 10-13 show the corresponding information for  $CO_2$  and  $H_2$ , respectively.

One aspect of the rarefied nature of these flows is that light molecular weight species tend to diffuse much more readily than the heavier species. To some extent this is evident in comparing the  $H_2$  to the  $H_2O$  or  $CO_2$  column densities in the previous figures. The point can be seen more clearly in Figure 14, which compares the  $H_2$  and  $H_2O$  number densities at a position 2.1 km downstream from the exit plane for the 200 km,  $0^\circ$  case. Although the exhaust contains approximately twice as much  $H_2O$  as  $H_2$  (Table 1),  $[H_2O] = 2.8[H_2]$  on the axis, and  $0.39[H_2]$  on the edge of the plot. The enhanced diffusion of the  $H_2$  causes it to be relatively depleted in the dense regions, and relatively more dominant in the wing regions. As will be seen, this behavior can also have implications for radiation contamination.

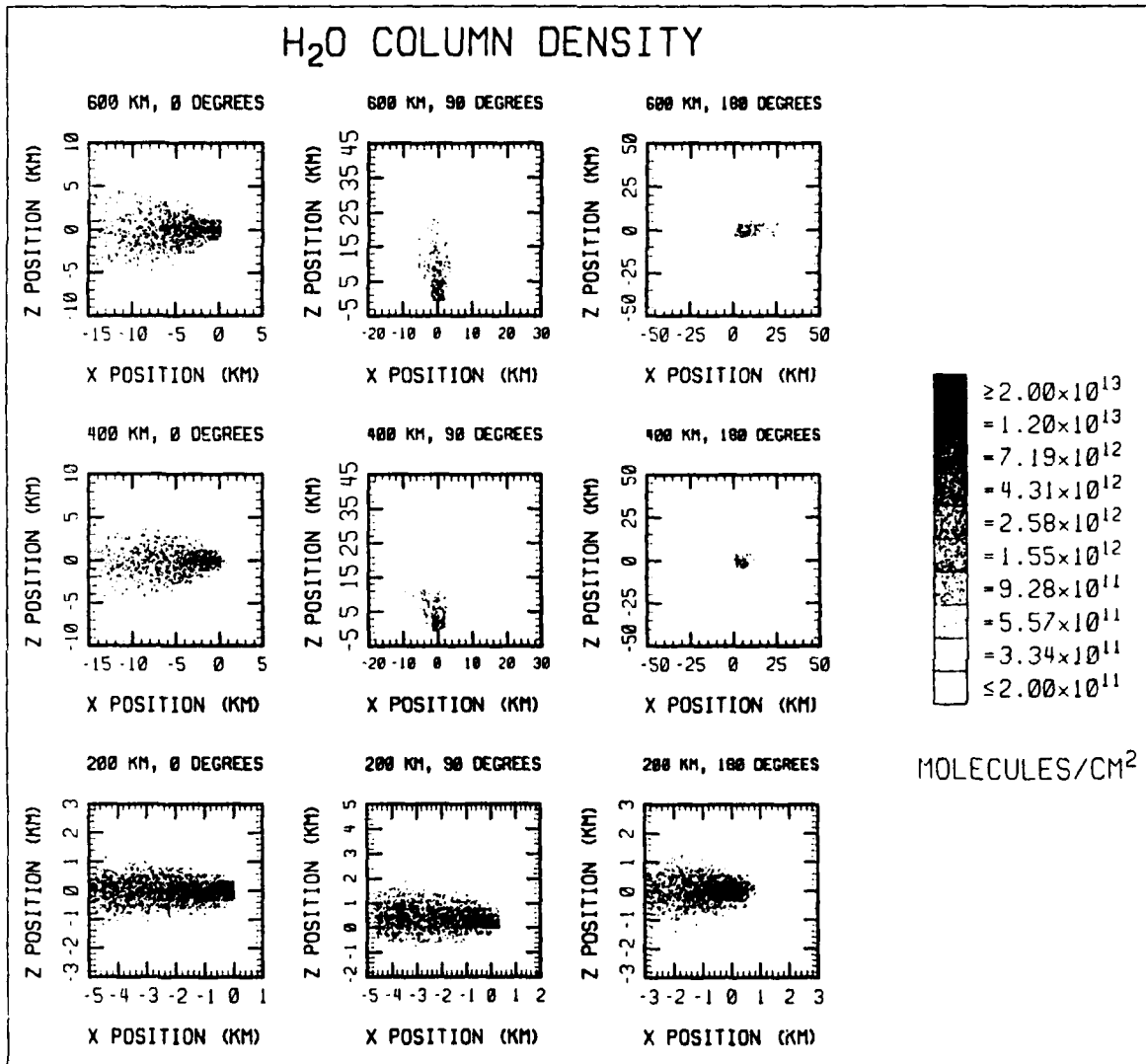


Figure 2. A panel of gray scale plots showing the H<sub>2</sub>O column density resulting from VRCS firings at 200, 400, and 600 Km, each at three angles of attack: 0, 90, and 180°.

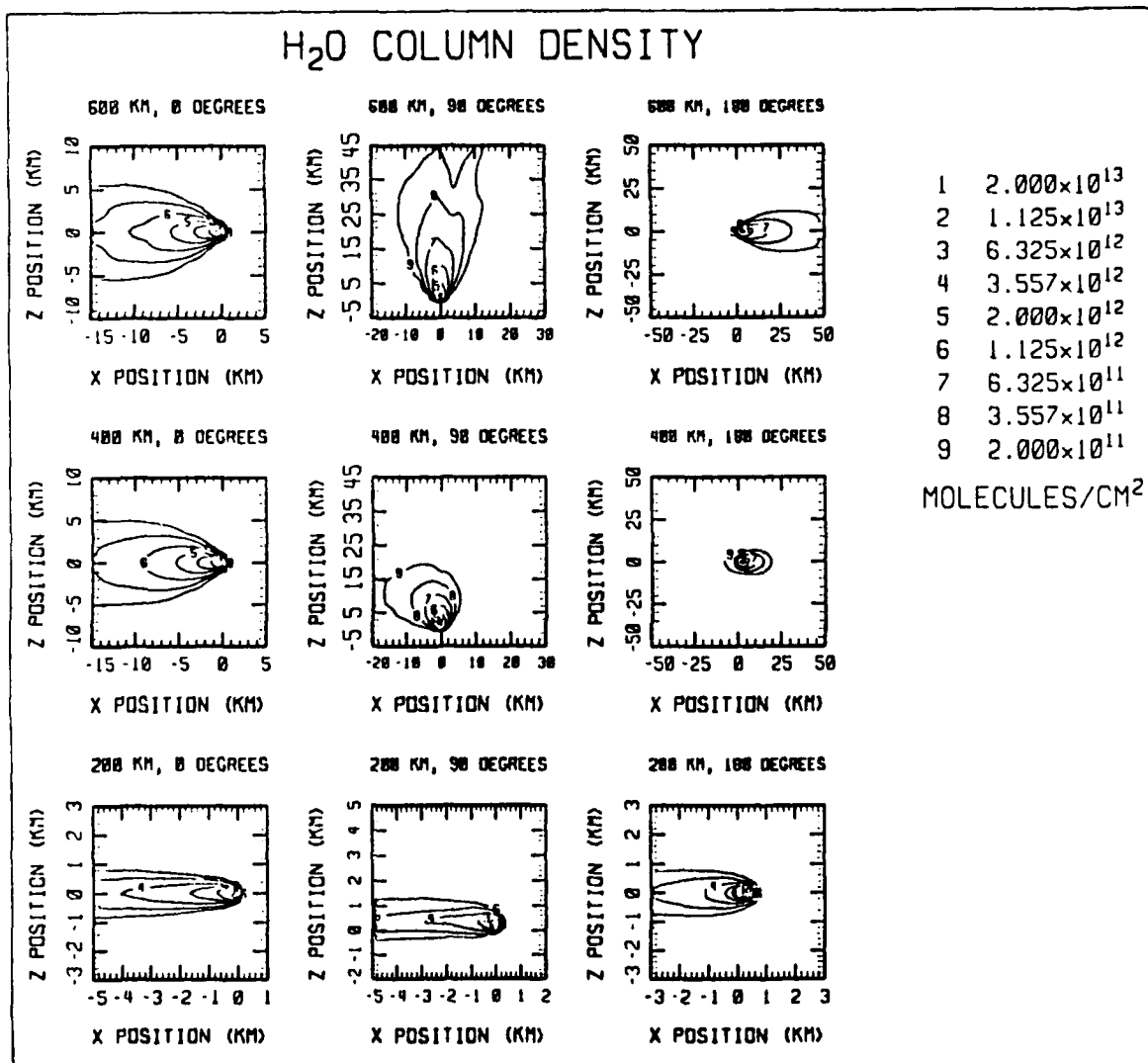


Figure 3. A panel of contour plots showing the H<sub>2</sub>O column density resulting from VRCs firings at 200, 400, and 600 Km, each at three angles of attack: 0, 90, and 180°.

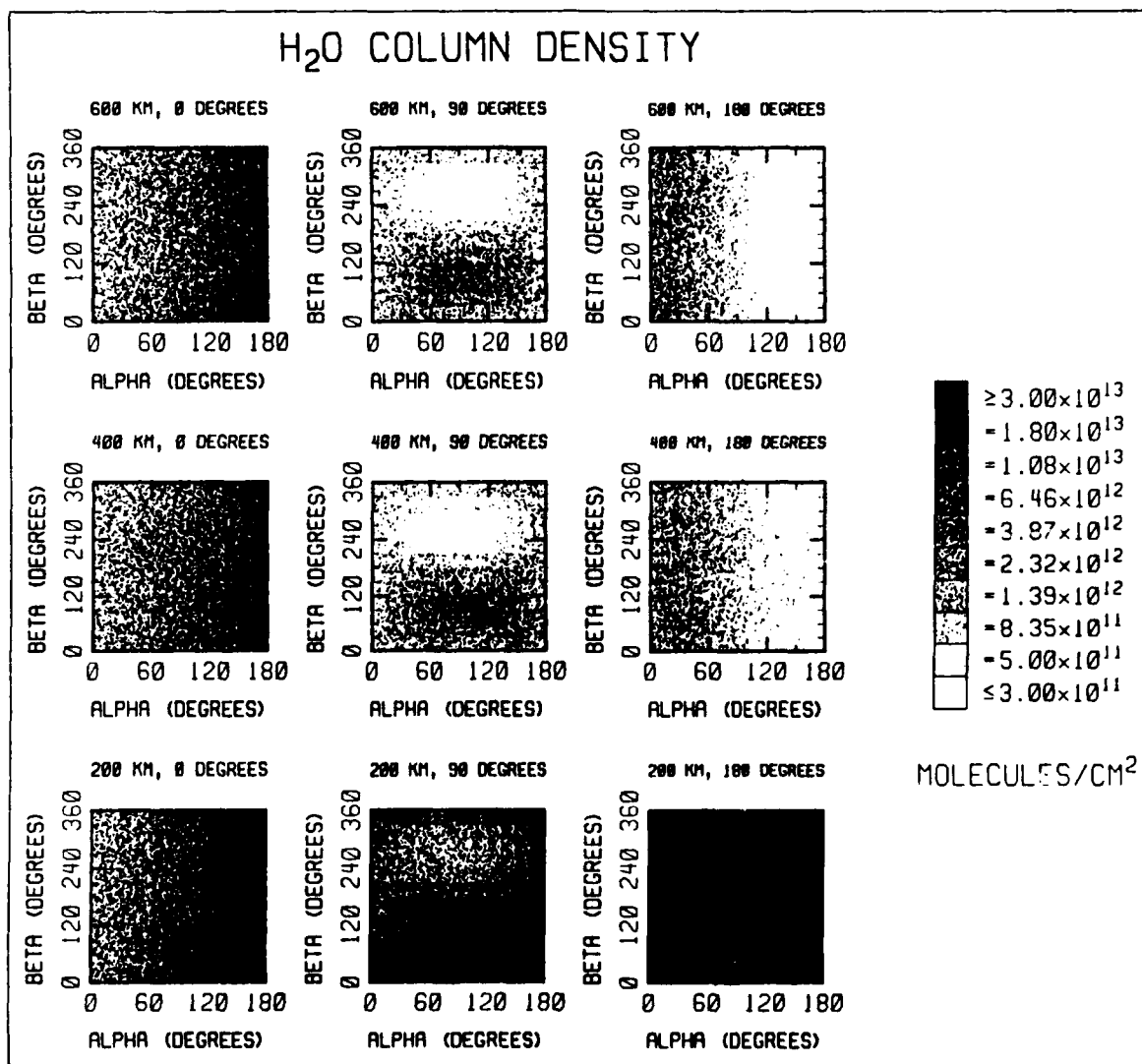


Figure 4. A panel of gray scale plots showing the H<sub>2</sub>O column density resulting from VRCS firings at 200, 400, and 600 Km, each at three angles of attack: 0, 90, and 180°. The column density is shown as a function of look angles for different viewing directions from the shuttle bay.

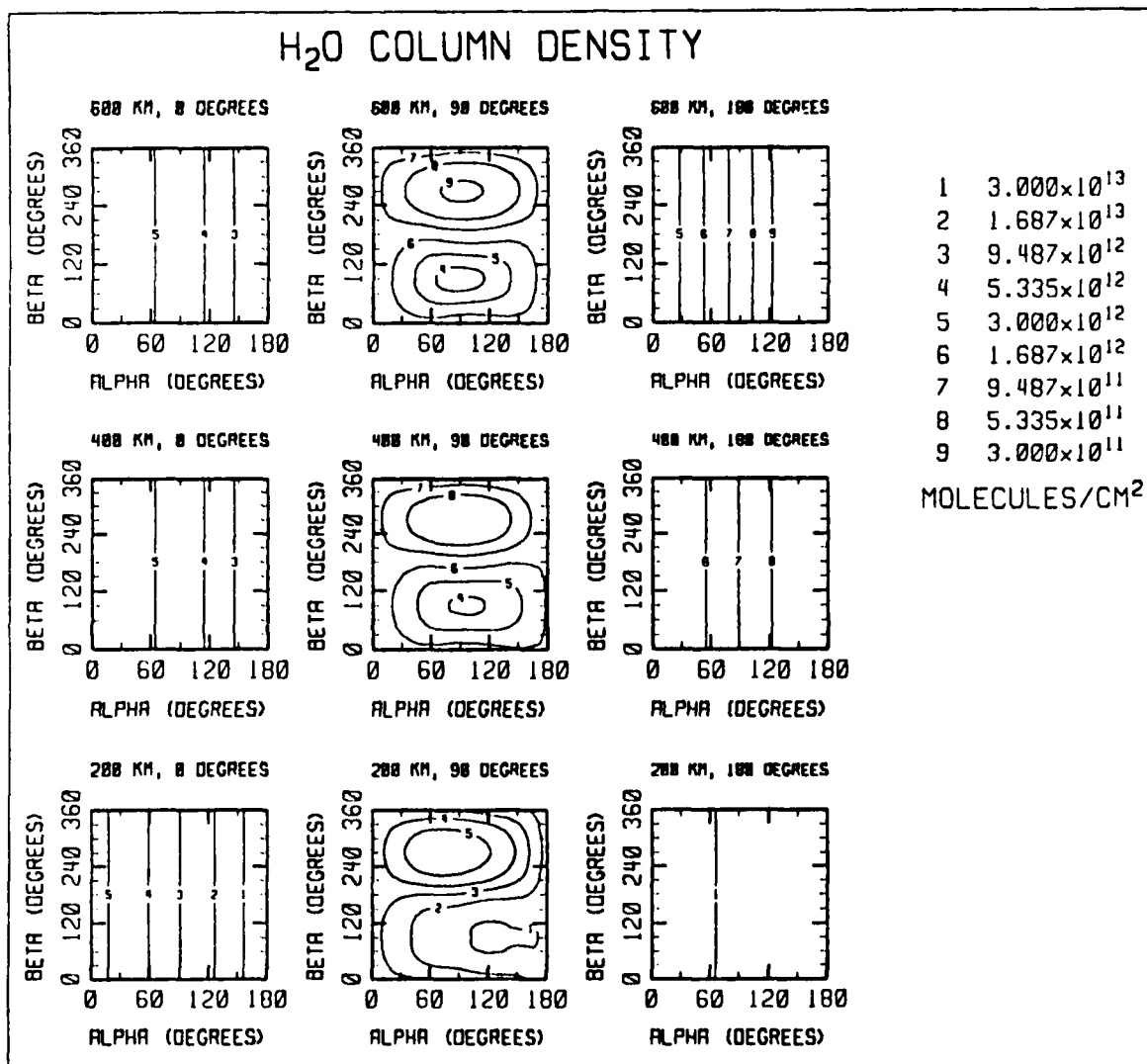


Figure 5. A panel of contour plots showing the H<sub>2</sub>O column density resulting from VRCS firings at 200, 400, and 600 Km, each at three angles of attack: 0, 90, and 180°. The column density is shown as a function of look angles for different viewing directions from the shuttle bay.

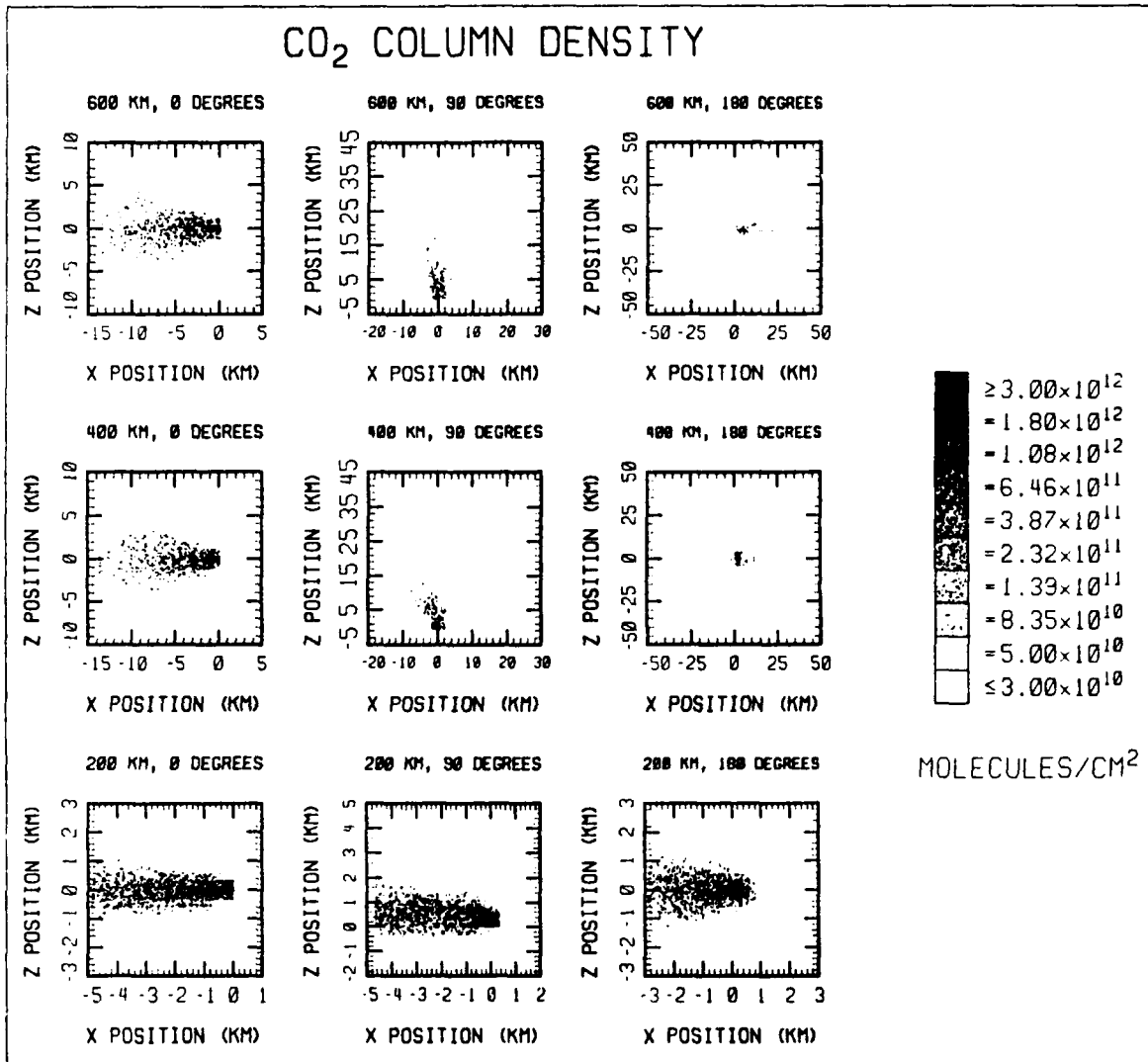


Figure 6. A panel of gray scale plots showing the CO<sub>2</sub> column density resulting from VRCS firings at 200, 400, and 600 Km, each at three angles of attack: 0, 90, and 180°.

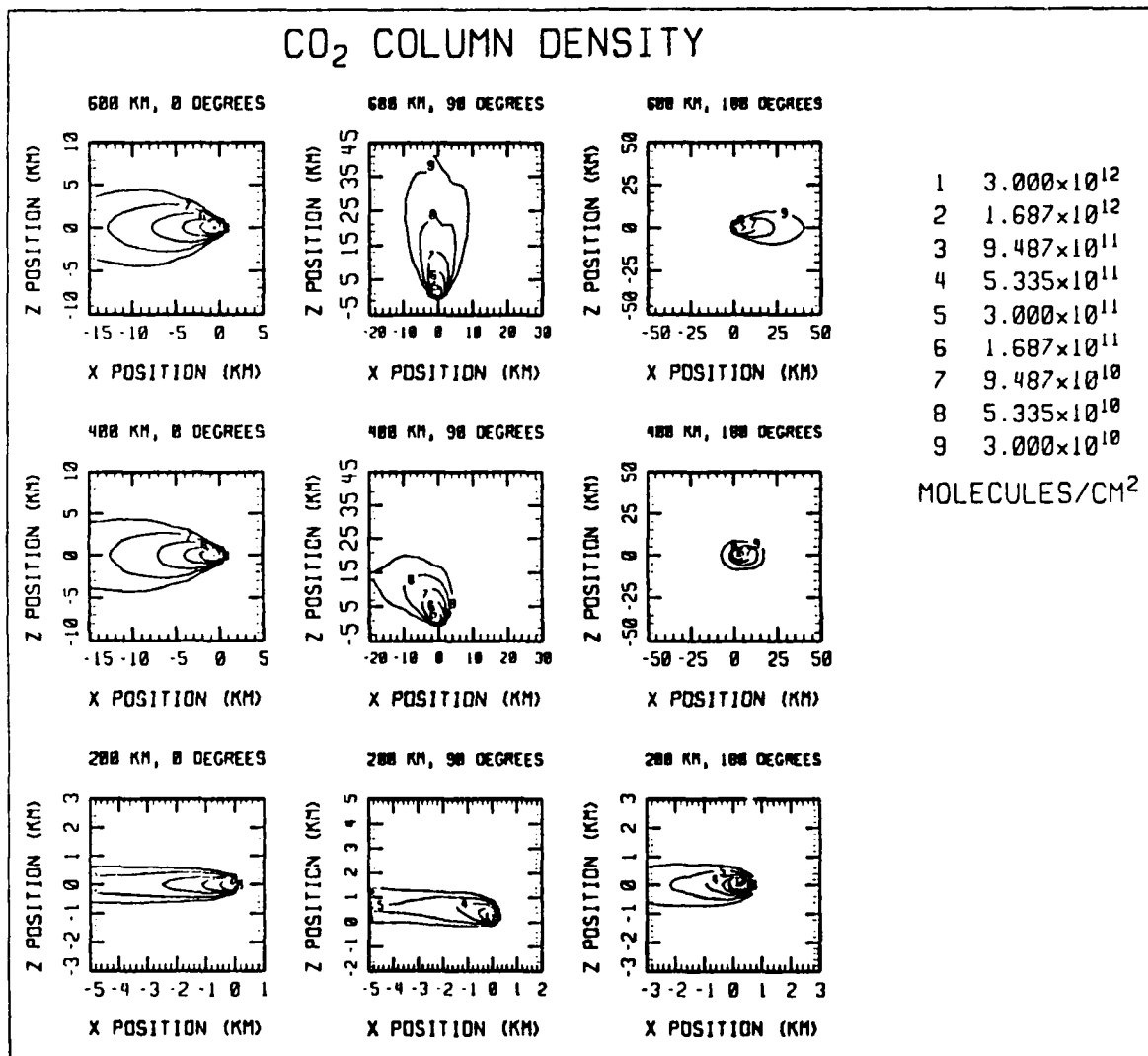


Figure 7. A panel of contour plots showing the CO<sub>2</sub> column density resulting from VRCS firings at 200, 400, and 600 Km, each at three angles of attack: 0, 90, and 180°.



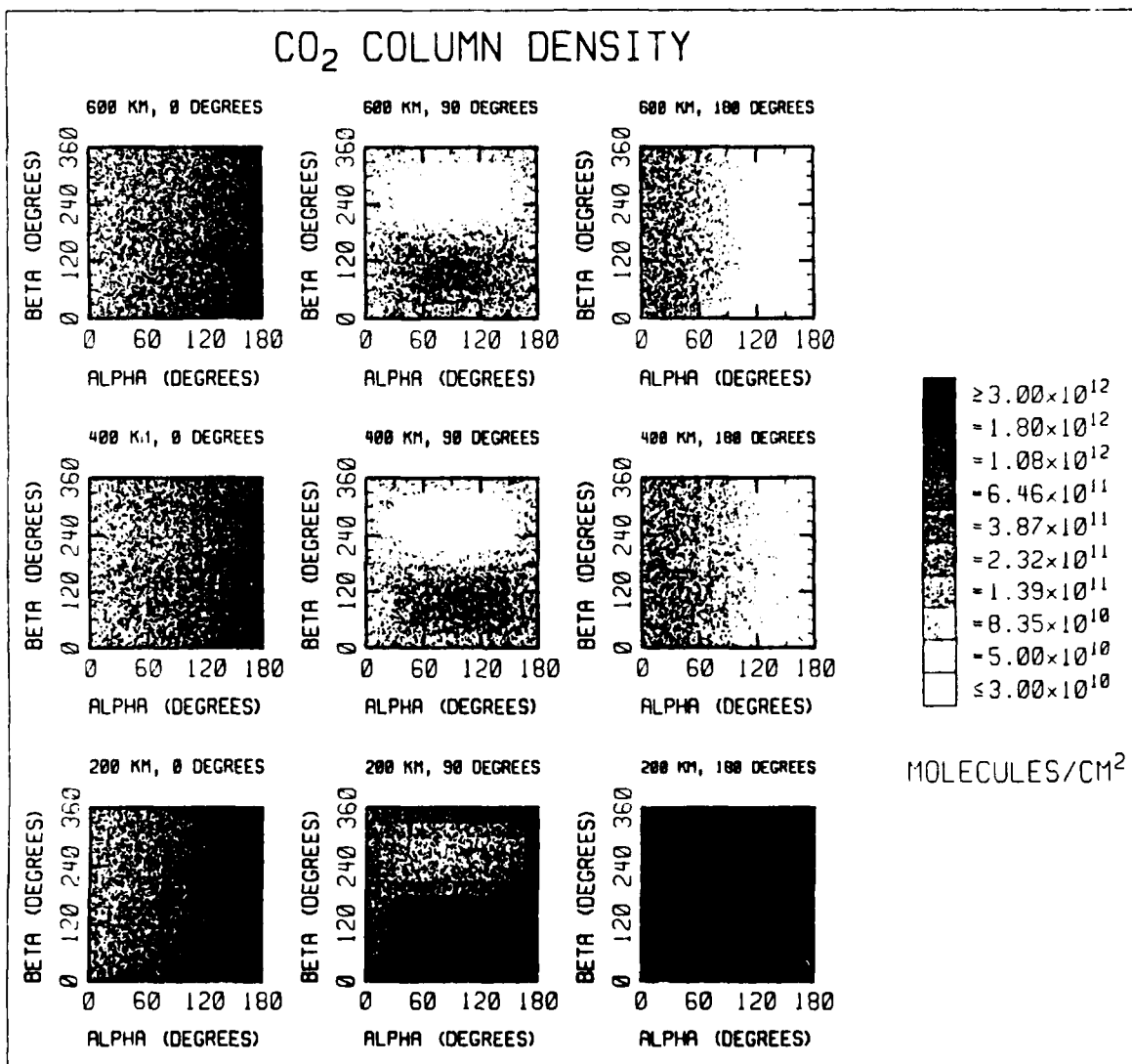


Figure 8. A panel of gray scale plots showing the CO<sub>2</sub> column density resulting from VRCS firings at 200, 400, and 600 Km, each at three angles of attack: 0, 90, and 180°. The column density is shown as a function of look angles for different viewing directions from the shuttle bay.

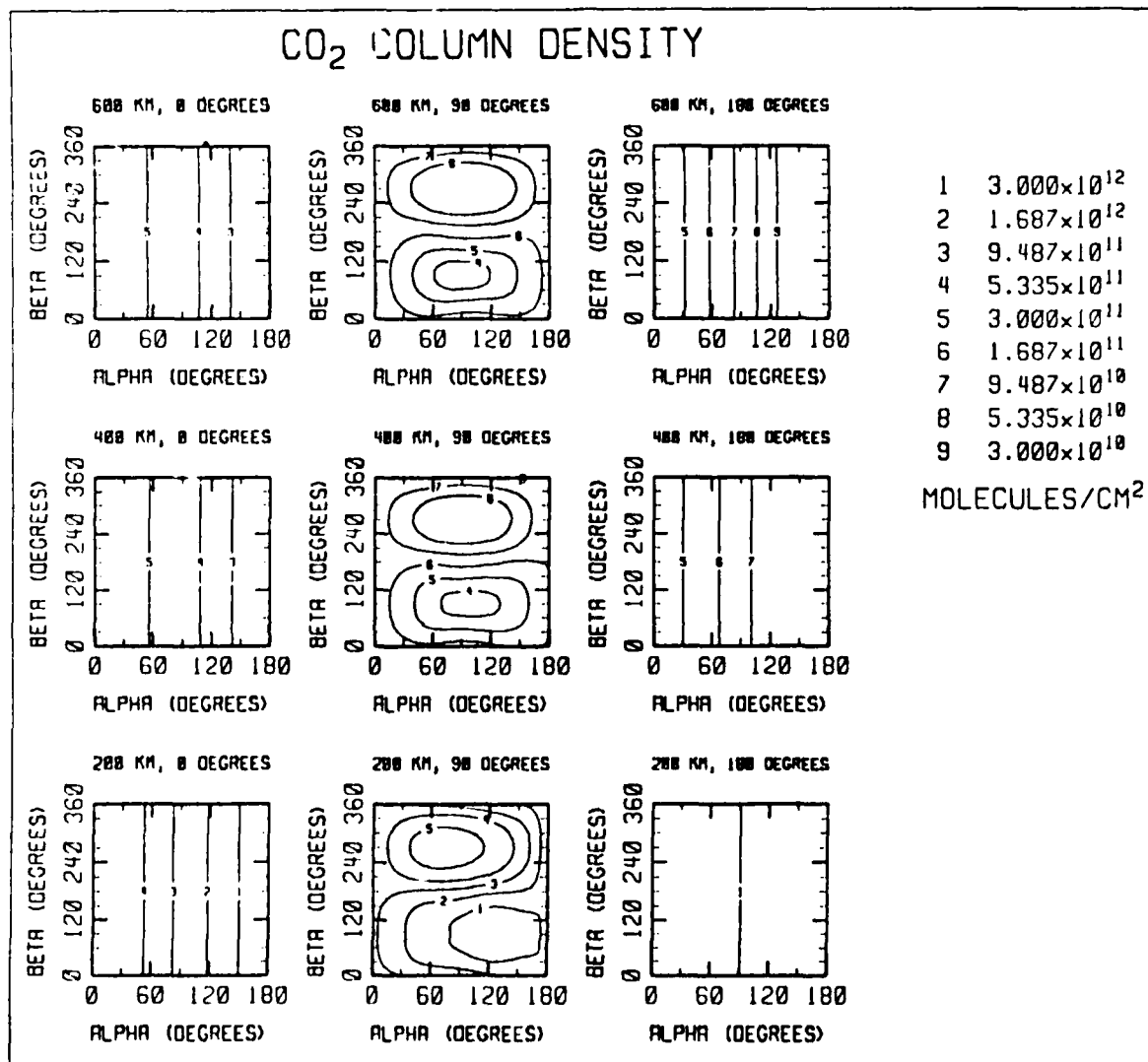


Figure 9. A panel of contour plots showing the CO<sub>2</sub> column density resulting from VRCS firings at 200, 400, and 600 Km, each at three angles of attack: 0, 90, and 180°. The column density is shown as a function of look angles for different viewing directions from the shuttle bay.

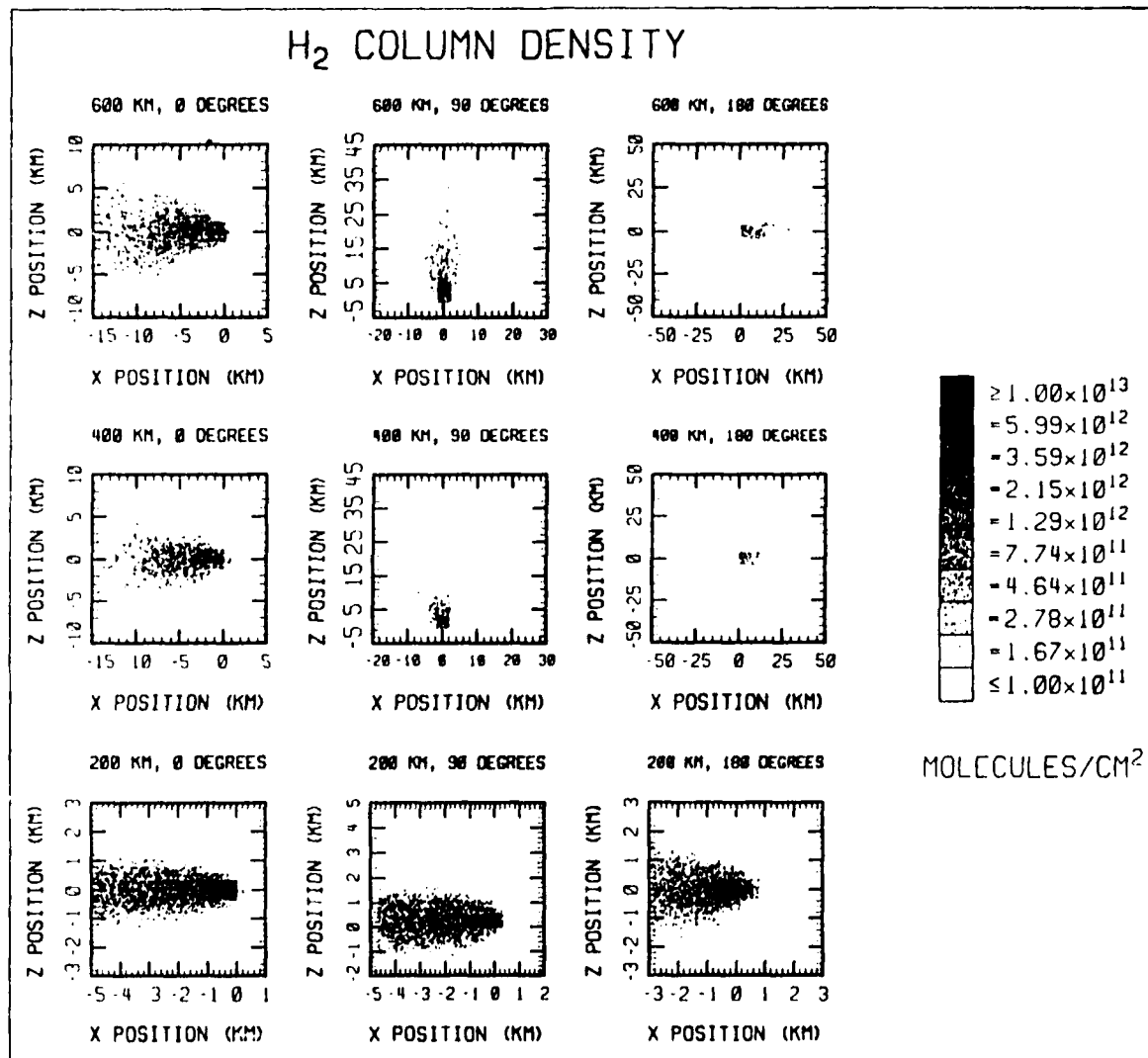


Figure 10. A panel of gray scale plots showing the H<sub>2</sub> column density resulting from VRCS firings at 200, 400, and 600 Km, each at three angles of attack: 0, 90, and 180°.

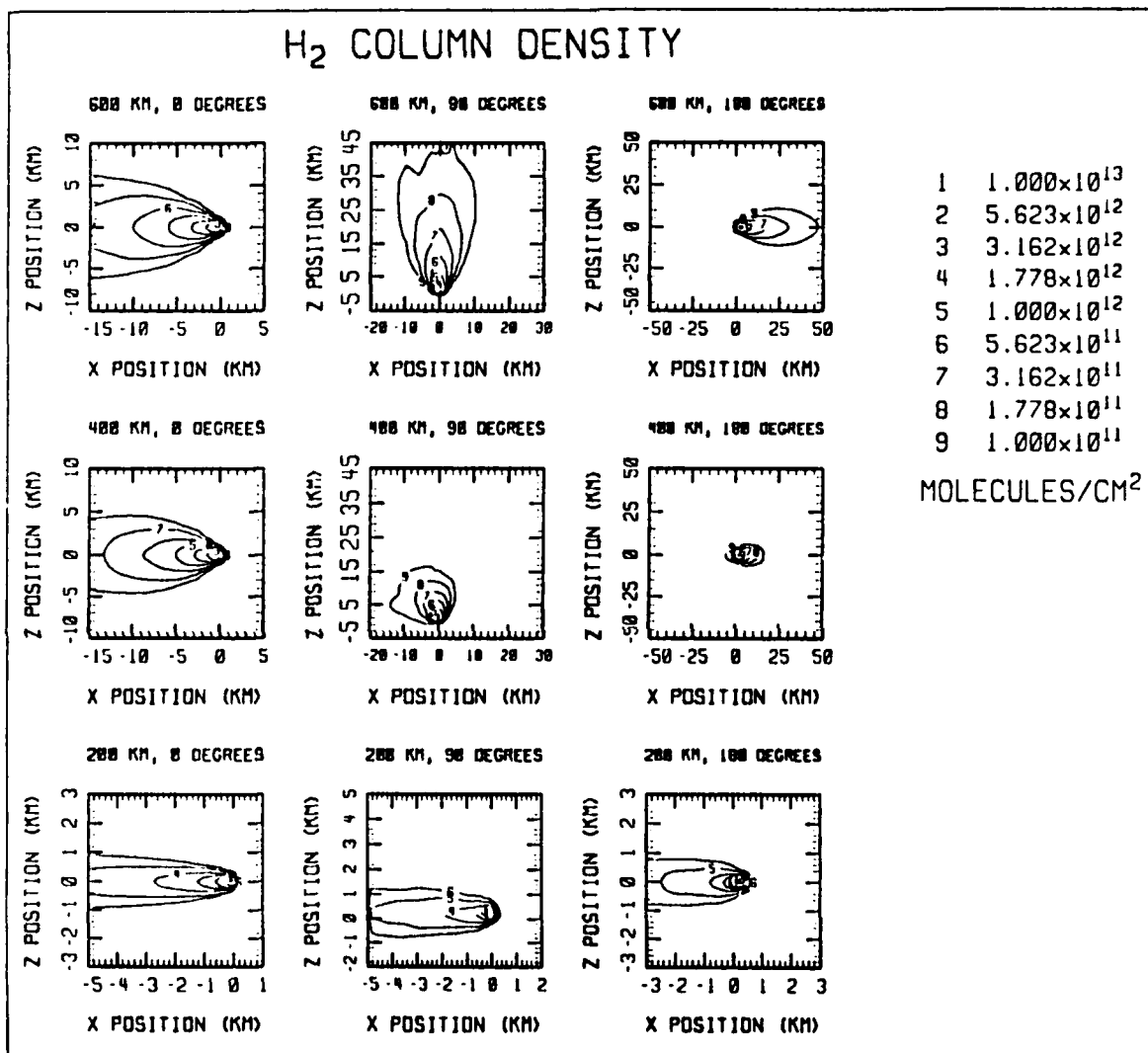


Figure 11. A panel of contour plots showing the H<sub>2</sub> column density resulting from VRCS firings at 200, 400, and 600 Km, each at three angles of attack: 0, 90, and 180°.

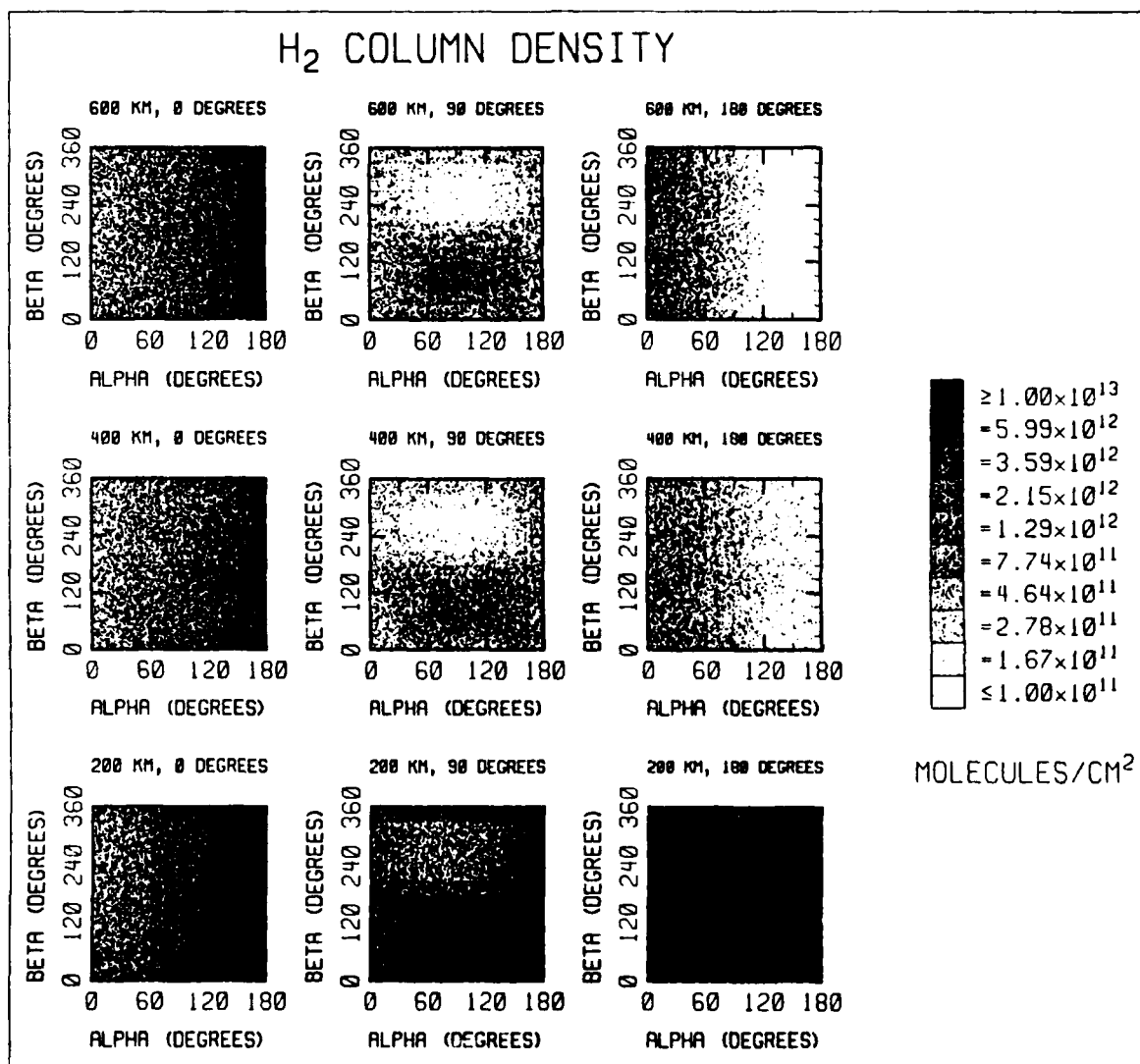


Figure 12. A panel of gray scale plots showing the H<sub>2</sub> column density resulting from VRCS firings at 200, 400, and 600 Km, each at three angles of attack: 0, 90, and 180°. The column density is shown as a function of look angles for different viewing directions from the shuttle bay.

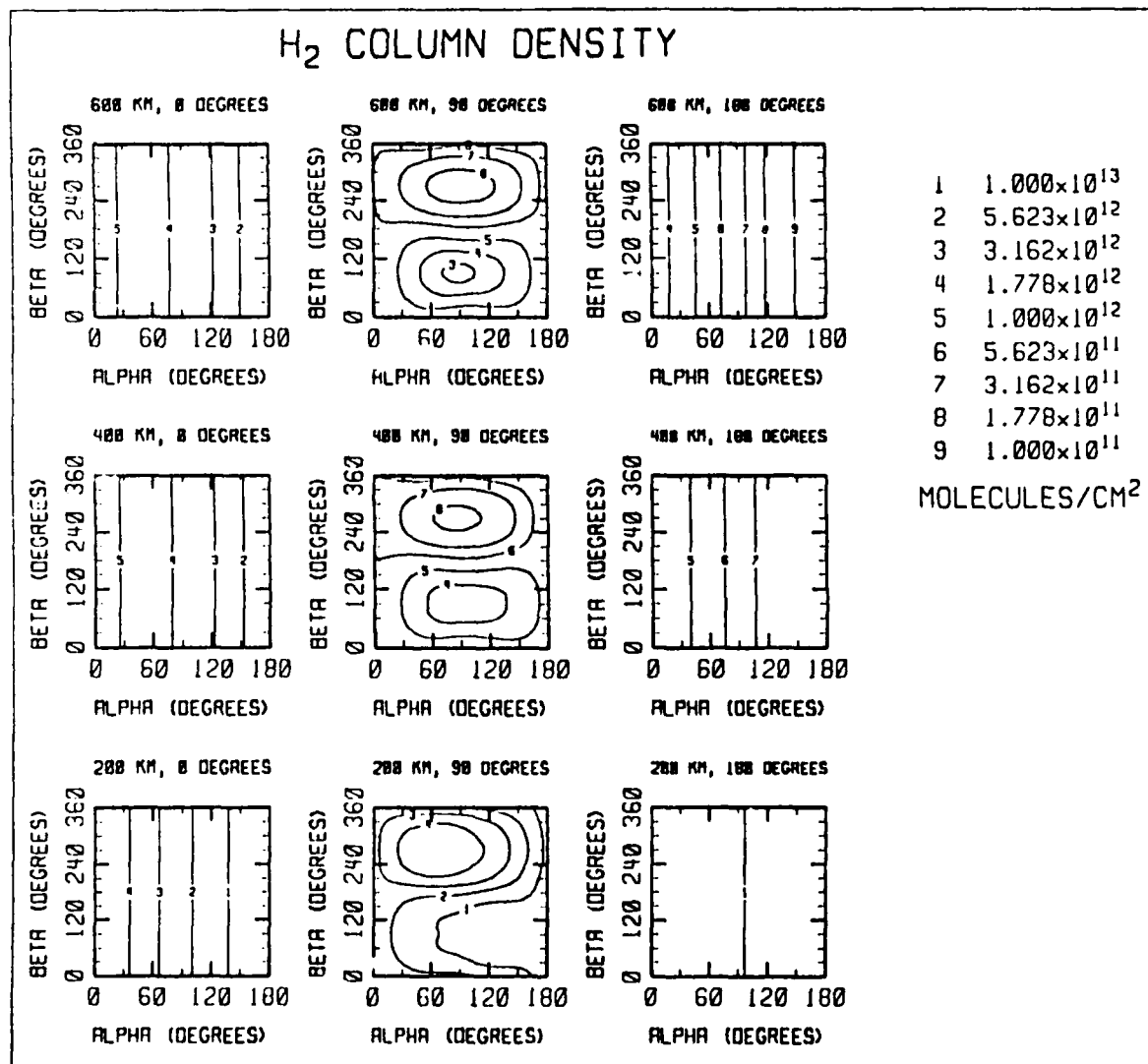


Figure 13. A panel of contour plots showing the H<sub>2</sub> column density resulting from VRCS firings at 200, 400, and 600 Km, each at three angles of attack: 0, 90, and 180°. The column density is shown as a function of look angles for different viewing directions from the shuttle bay.

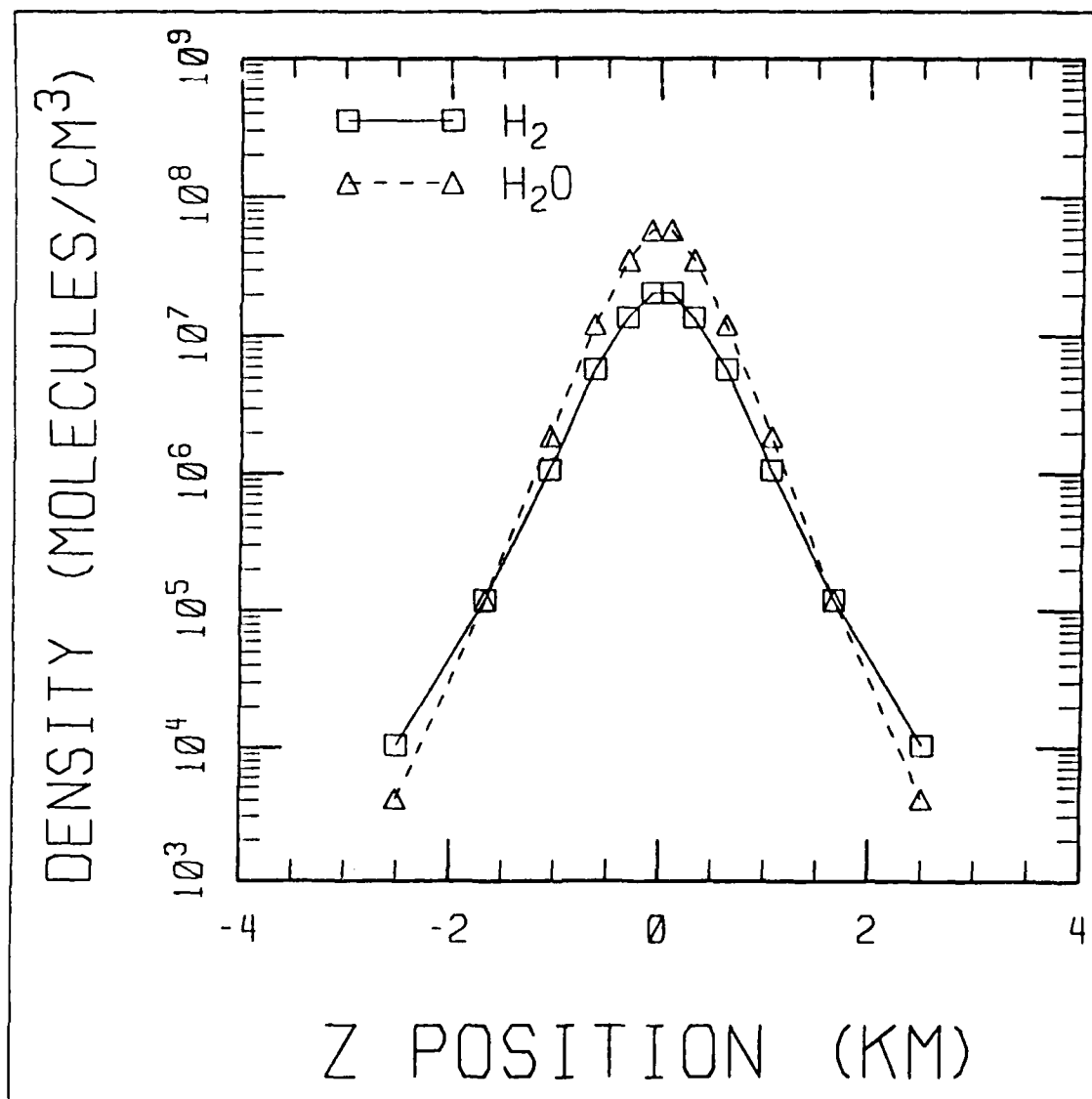


Figure 14. A comparison of the H<sub>2</sub> and H<sub>2</sub>O number densities at an altitude of 200 Km and 0° angle of attack for a position 2.1 km downstream from the exit plane.

#### 4. T-V COLLISIONS

An important channel for absorbing the high collision energy between the ambient O atoms and the plume is the collisional excitation of vibrational modes of plume molecules (particularly the heteronuclear molecules), e.g.



This reaction has been studied both theoretically and experimentally, and found to be very fast<sup>(17-19)</sup> In this work we have used the value  $k_2 = [1.2 \times 10^{-16} T^{1.34} e^{(-10730/kT)}]$  (Ref. 5). Using this rate coefficient and the known 17 msec radiative lifetime of  $H_2O(\nu_3=1)$  we can calculate the contours of the  $2.7\mu$  radiation caused by the interaction of fast O atoms with  $H_2O$  from the plume. This is shown in Figures 15-18, again for all the cases considered. In a similar fashion we can calculate the emission in the  $4.3\mu$  band excited by the collision between fast ambient O atoms with  $CO_2$  in the exhaust of the VRCS engines:



Here, the rate coefficient,  $k_4$ , is less well known and we have used  $k_4 = [3.5 \times 10^{-16} T^{2.18} e^{(-6.74/kT)}]$  (Ref. 5). The results are presented in Figures 19-22.

The gray scale utilized in these figures encompasses five orders of magnitude, versus two for the column density figures of the previous section. The reason for this is that there is a well defined vacuum limit for species densities, whereas the collisionally induced emission depends on an interaction with the atmosphere, and becomes increasingly tenuous as the altitude is increased. The spatial extent of the emission at 0 and 90 degrees angle of attack is greater than the density, however, even without



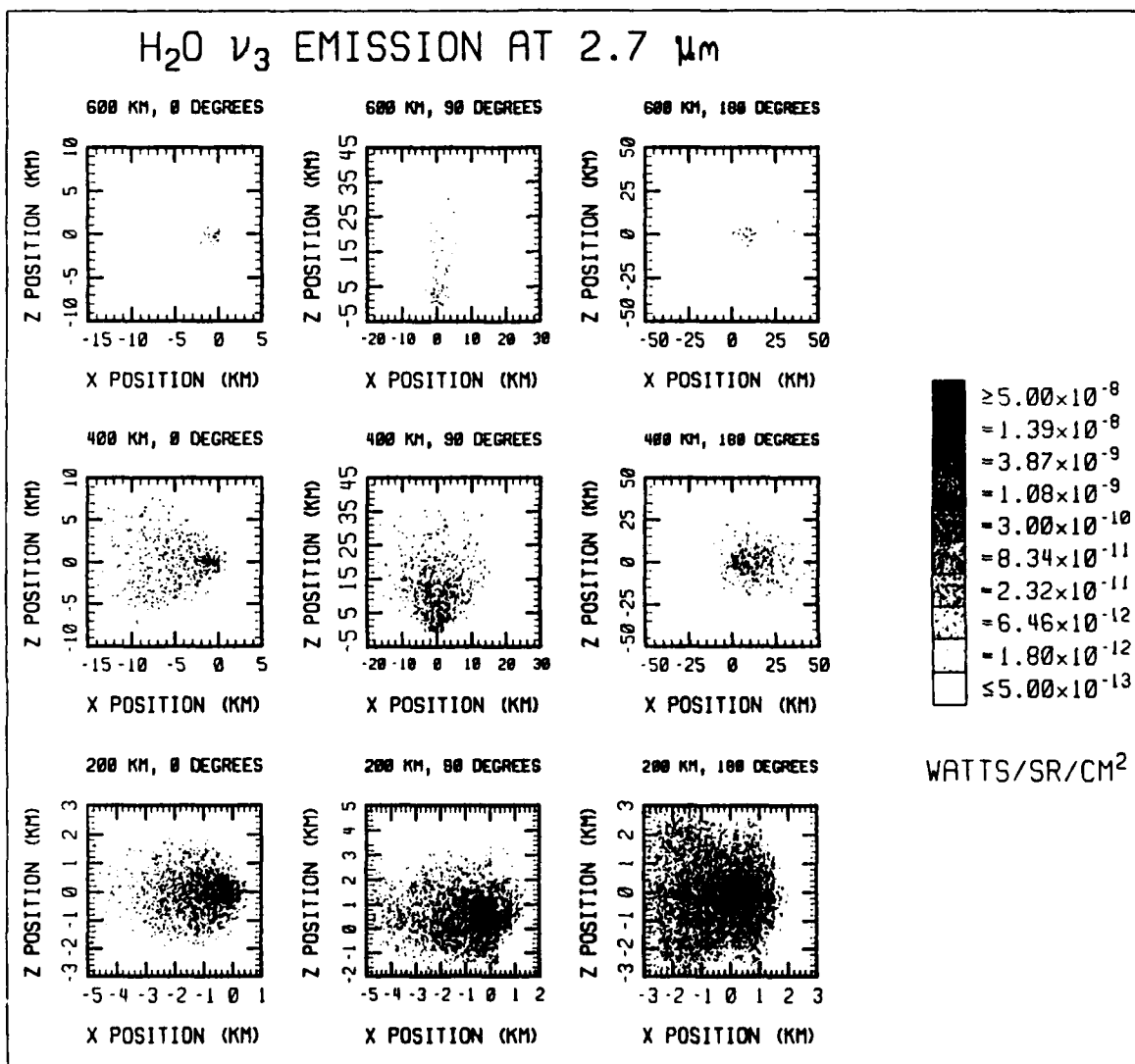


Figure 15. A panel of gray scale plots showing the H<sub>2</sub>O  $\nu_3$  emission at 2.7  $\mu\text{m}$  due to excitation from collisions with atomic oxygen.

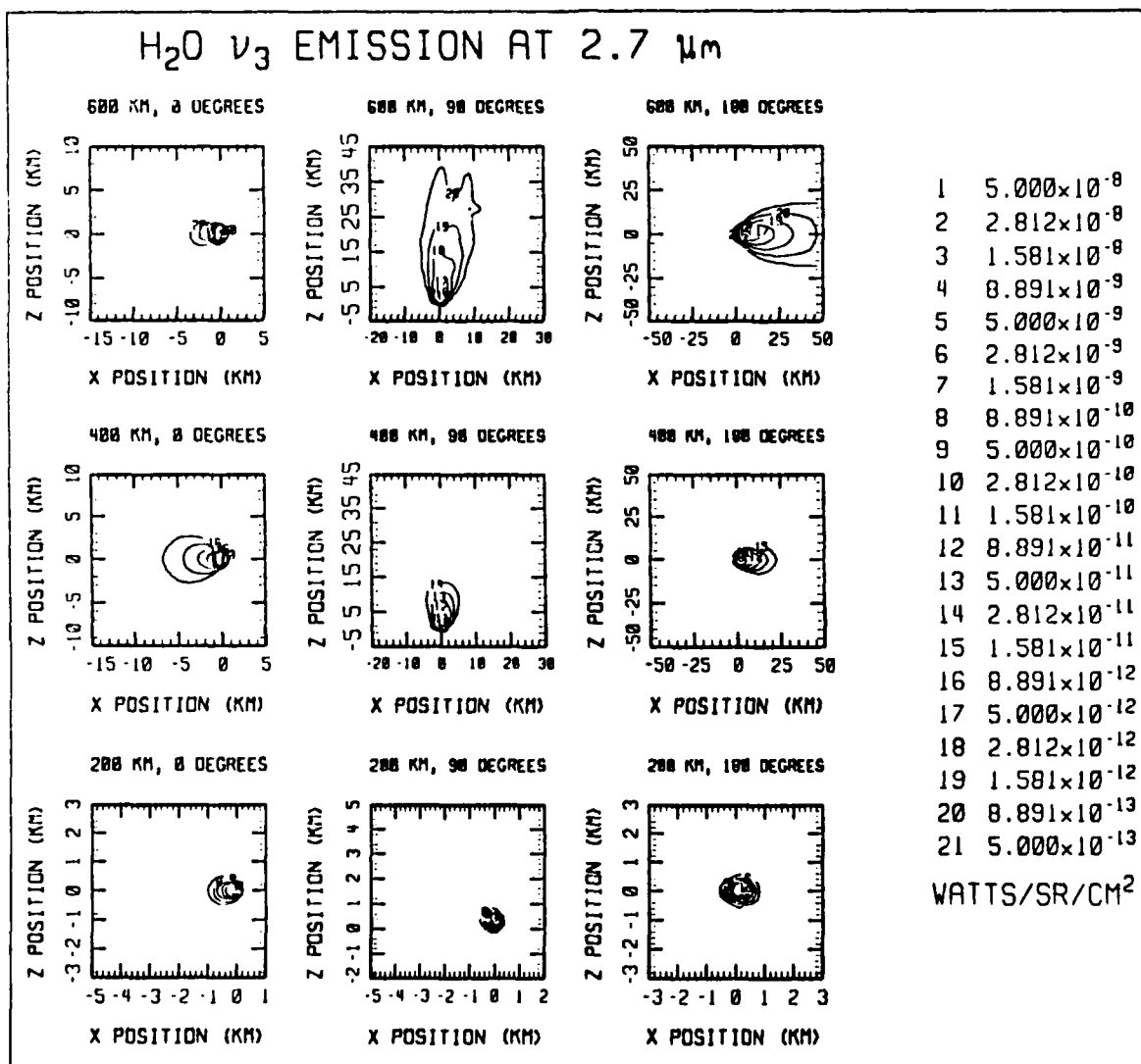


Figure 16. A panel of contour plots showing the H<sub>2</sub>O  $\nu_3$  emission at 2.7  $\mu\text{m}$  due to excitation from collisions with atomic oxygen.

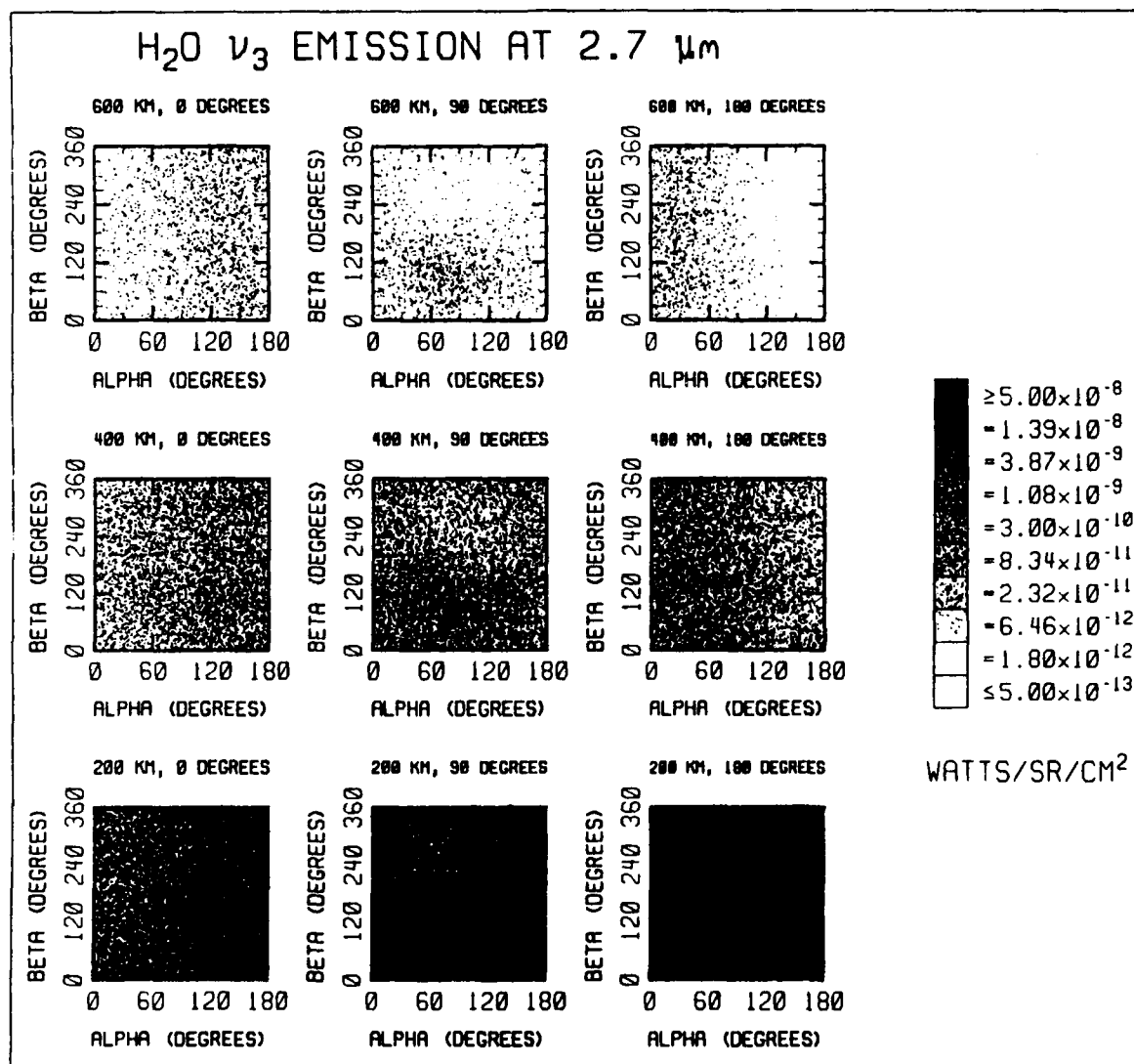


Figure 17. A panel of gray scale plots showing the H<sub>2</sub>O  $\nu_3$  emission at 2.7  $\mu\text{m}$  due to excitation from collisions with atomic oxygen. The emission is shown as a function of look angles for different viewing directions from the shuttle bay.

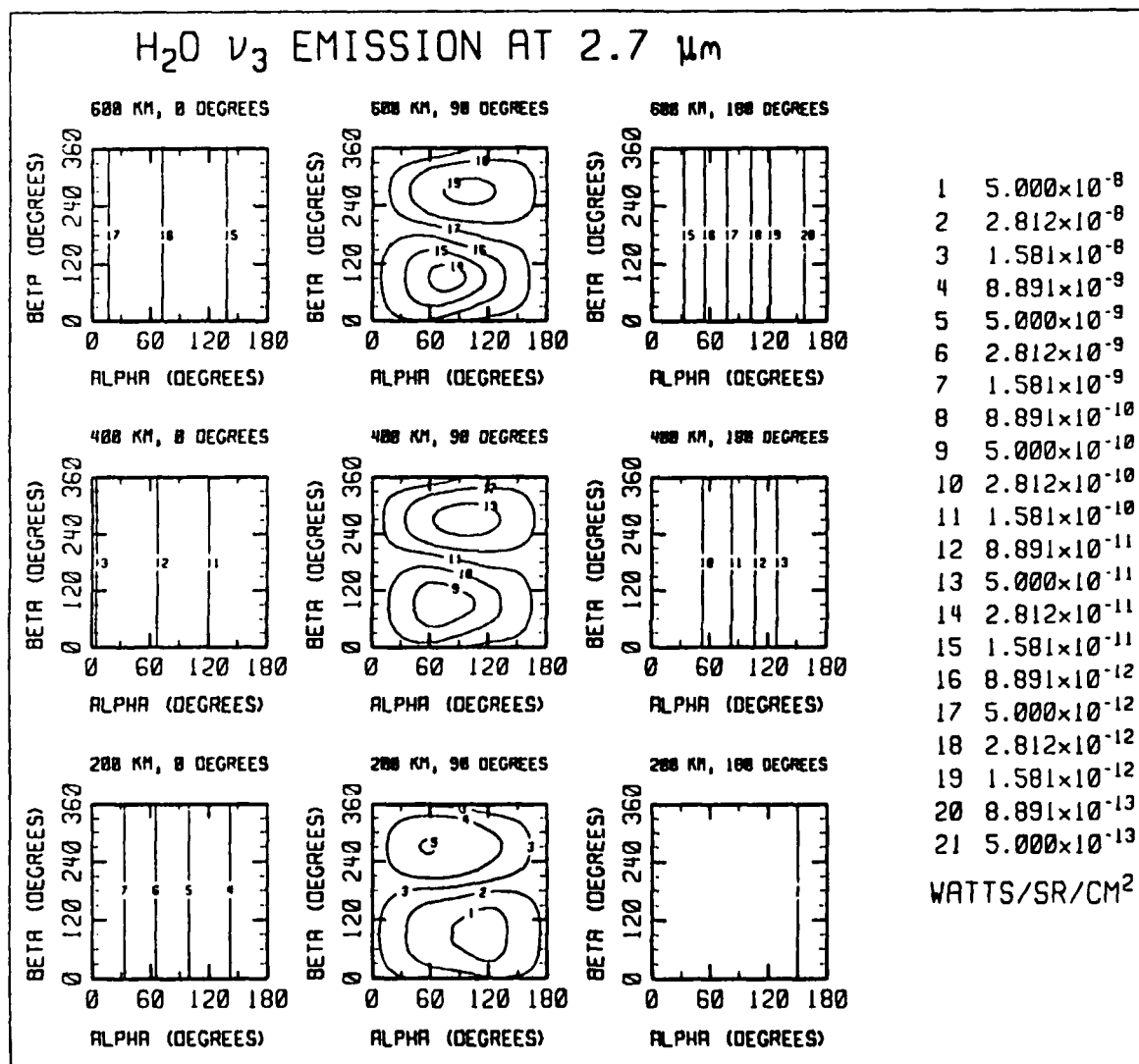


Figure 18. A panel of contour plots showing the H<sub>2</sub>O  $\nu_3$  emission at 2.7  $\mu\text{m}$  due to excitation from collisions with atomic oxygen. The emission is shown as a function of look angles for different viewing directions from the shuttle bay.

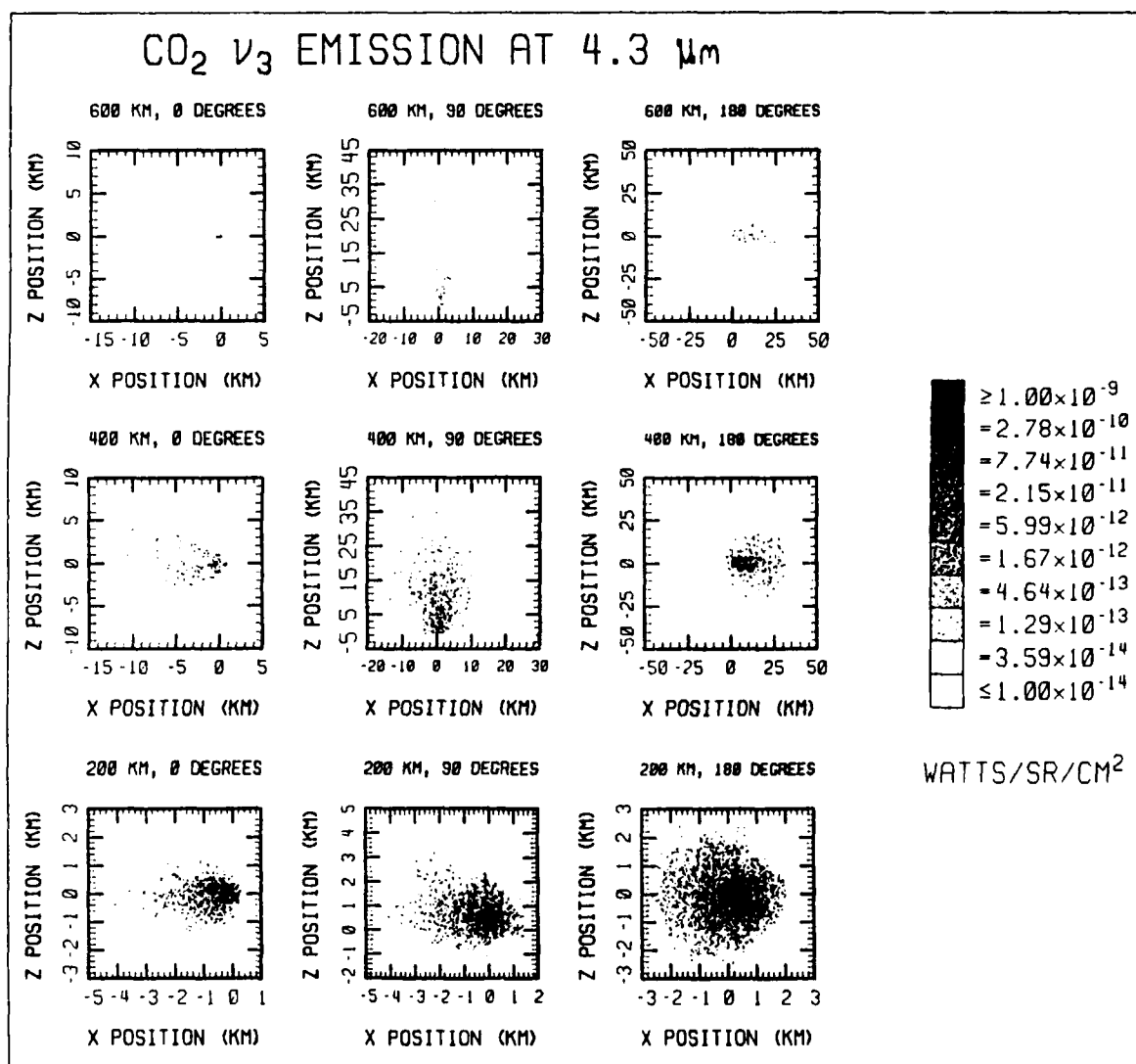
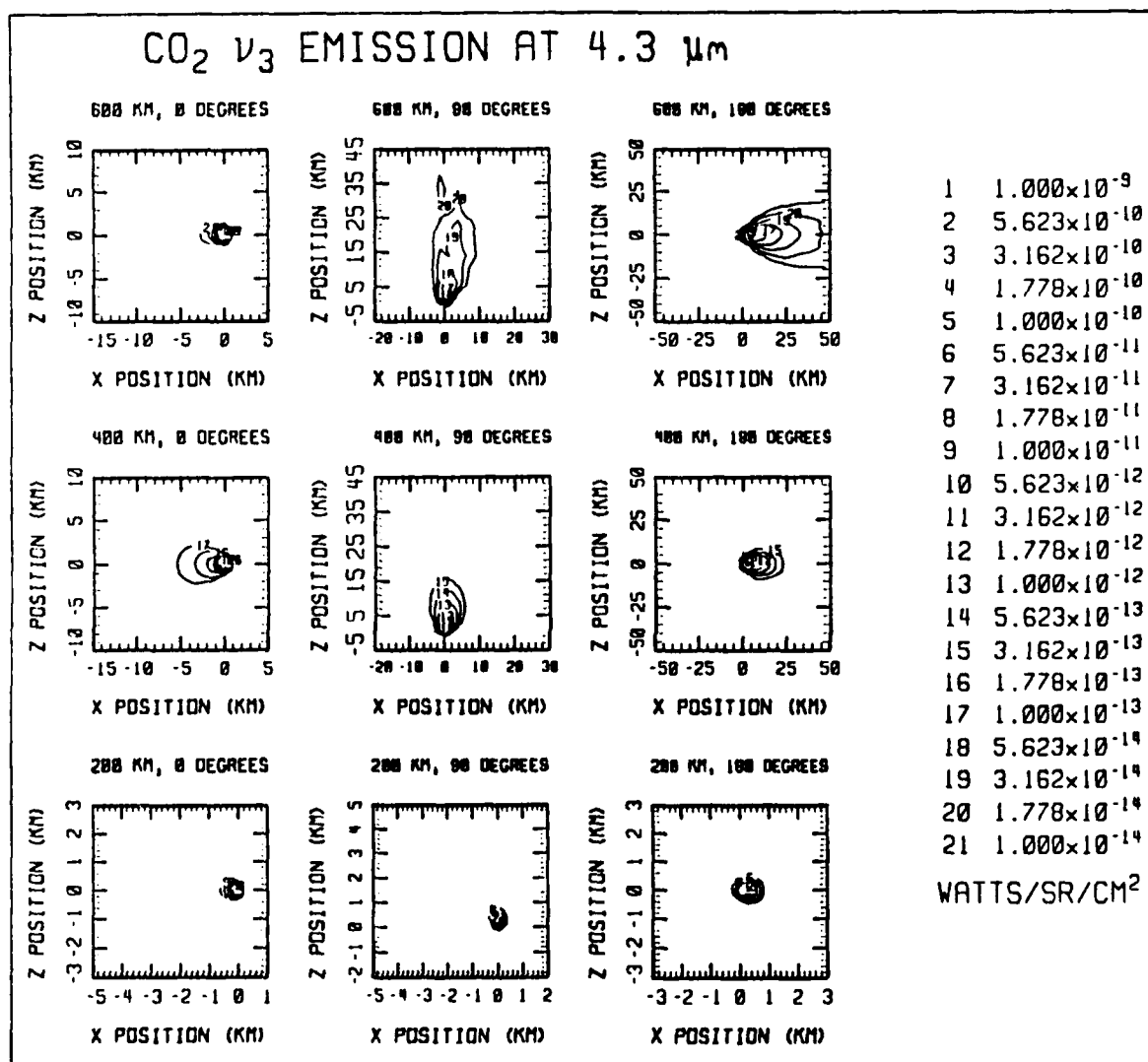


Figure 19. A panel of gray scale plots showing the CO<sub>2</sub>  $\nu_3$  emission at 4.3  $\mu\text{m}$  due to excitation from collisions with atomic oxygen.



**Figure 20. A panel of contour plots showing the CO<sub>2</sub>  $\nu_3$  emission at 4.3  $\mu\text{m}$  due to excitation from collisions with atomic oxygen.**

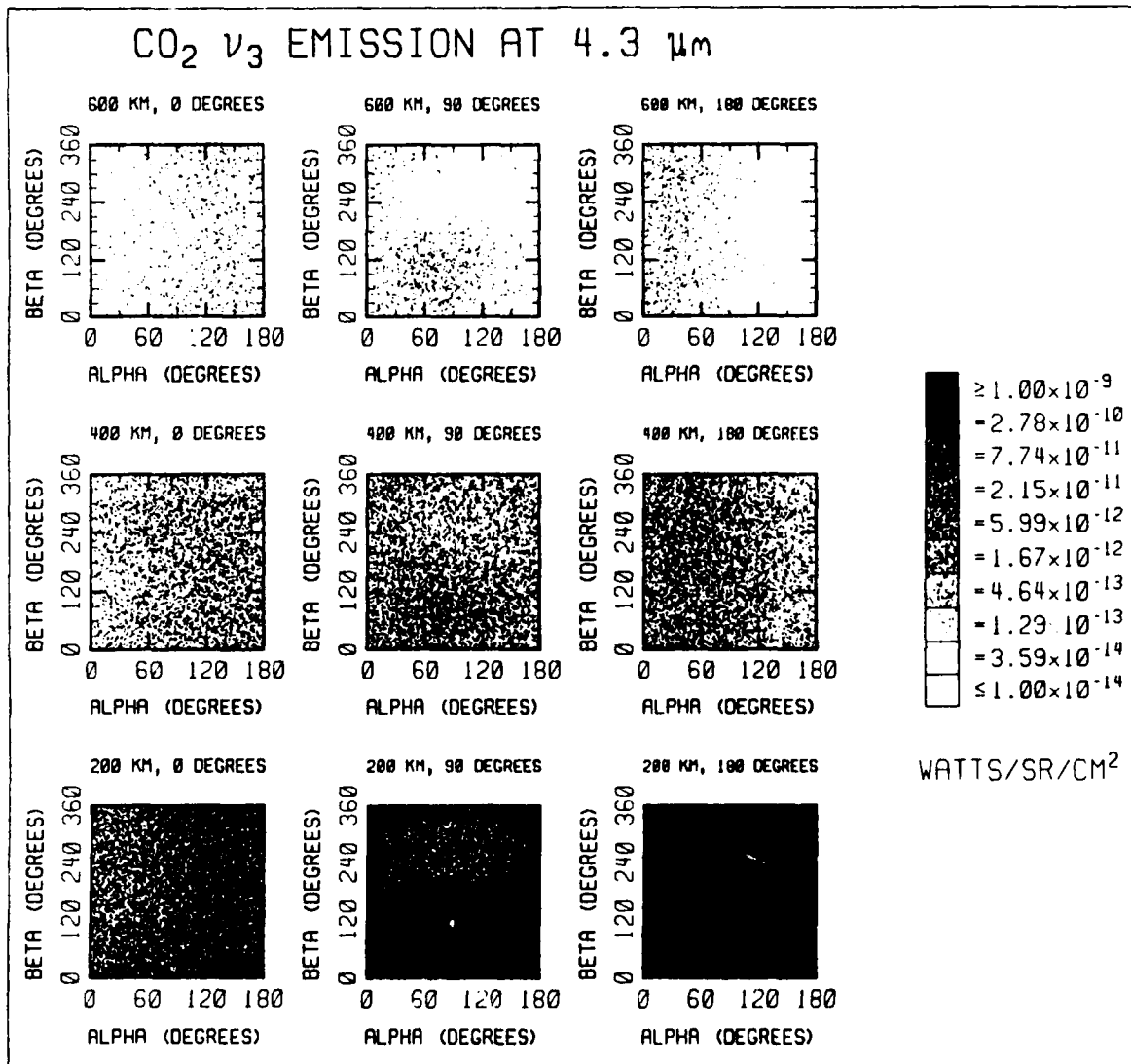


Figure 21. A panel of gray scale plots showing the CO<sub>2</sub>  $\nu_3$  emission at 4.3  $\mu\text{m}$  due to excitation from collisions with atomic oxygen. The emission is shown as a function of look angles for different viewing directions from the shuttle bay.

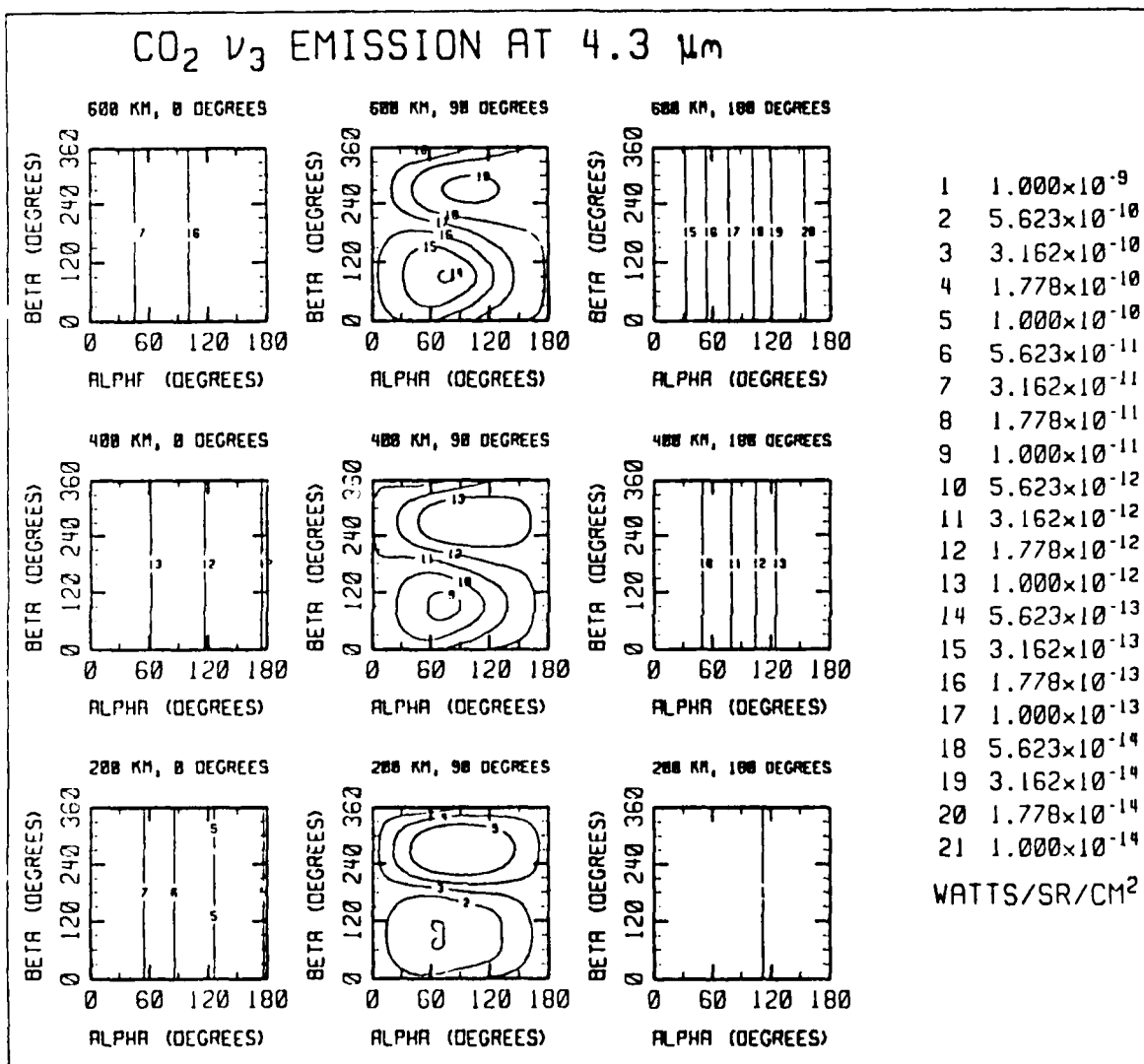


Figure 22. A panel of contour plots showing the CO<sub>2</sub>  $\nu_3$  emission at 4.3  $\mu\text{m}$  due to excitation from collisions with atomic oxygen. The emission is shown as a function of look angles for different viewing directions from the shuttle bay.



the scale change. This is because the small portion of the flow which has a relatively large initial upstream velocity component suffers higher energy collisions, and is more likely to produce emission. The importance of this portion of the flow is enhanced for collisionally induced emission relative to density.

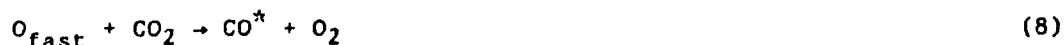
The total solution region emission for these processes is presented in Table 3. It can be seen that the effect of angle of attack is substantial for both mechanisms, while altitude has a lesser effect between 200 and 400 km. For the 600 km cases, there is substantial radiation outside of the solution region, though it is spread over such a vast region that the neglected portion is not important.

Table 3  
Total Solution Region Emission (Watts/Sr)

Case (Alt., A.O.A)	H <sub>2</sub> O( $\nu_3$ ) (2.7 $\mu$ )	CO <sub>2</sub> ( $\nu_3$ ) (4.3 $\mu$ )
200 Km, 0°	29.	0.28
200 Km, 90°	130.	1.7
200 Km, 180°	250.	4.0
400 Km, 0°	15.	0.14
400 Km, 90°	160.	2.3
400 Km, 180°	310.	6.2
600 Km, 0°	0.76	0.0082
600 Km, 90°	14.	0.22
600 Km, 180°	29.	0.58

## 5. REACTIVE COLLISIONS

We consider in this section the possibility that reactions which do not proceed at room temperature due to a large activation energy might become important in low earth orbit because of the orbital velocity. The reactions which we consider here represent species which are important exhaust products of VRCS engines:



There are some high temperature measurements for all three reactions. However, before we present the results of the calculations, a discussion of each of the reactions and the rate coefficients used is warranted.

Reaction (6): The reaction to produce ground state OH is endothermic by 0.73 eV, but at orbital velocity it has an excess energy of 1.86 eV ( $E_{CM}$  for  $O + H_2O$  at  $7.7 \text{ km s}^{-1}$  is 2.59 eV if the velocity of the exhaust is ignored. If the velocities are added, i.e. at  $\theta = 180^\circ$ , then the reaction has an excess energy of 4.5 eV). Since  $\omega_e$  for OH =  $3738 \text{ cm}^{-1}$  ( $2.7 \mu$  or 0.46 eV),  $OH^*$  can be formed at  $v'' \leq 3$  for the scenario where the exhaust is at  $90^\circ$  with respect to direction of travel. At  $180^\circ$  the reaction can excite OH into the A ( $^2\Sigma^+$ ) state, which lies at  $32684 \text{ cm}^{-1}$  (4.03 eV) above the ground state.<sup>(20)</sup> This possibility would lead to emission of intense ultraviolet-visible light, since the A-X transition is allowed, the radiative lifetime being 0.7  $\mu\text{s}$ .

The rate coefficient for this reaction has not been measured at energies corresponding to orbital energies. However, Albers et al.<sup>(21)</sup> have reported high temperature measurements which yield a rate coefficient,  $k_6$ , of  $-6.6 \times 10^{-11} e^{-(17300/KT)} \text{ cm}^3 \text{ molecule}^{-1} \text{ s}^{-1}$ . For the purpose of this work we have taken the available rate constant and adjusted the activation energy to account for the energy of the first vibrational state and (as a separate reaction) the A ( $^2\Sigma^+$ ) state.

Reaction (7): High temperature measurements by Miyauchi et al.<sup>(22)</sup> give  $k_7 = 3 \times 10^{-14} \text{Te}^{-(4480/T)} \text{ cm}^3 \text{ molec s}^{-1}$ . Other measurements have been reported by Schott et al.,<sup>(23)</sup> Pamidimukkala and Skinner,<sup>(24)</sup> and by Marshall and Fontijn<sup>(25)</sup> with slightly varying results. We have used the data of Miyauchi et al. The reaction is endothermic by 0.09 eV, while in low earth orbit it has an excess energy of 0.45 eV at 90° collision and 0.9 eV at 180° collisions. Thus only vibrationally excited OH can be formed. For the purpose of this calculation we have also adjusted the activation energy to reflect the energy of the first vibrational state.

Reaction (8): This reaction is endothermic by 0.33 eV. At orbital velocity and at 90° collision angle it has an excess energy of 3.26 eV, while at 180° collision angle it has an excess energy of 4 eV. In either case, the energy is not enough to form either O<sub>2</sub> or CO in excited electronic states. Vibrational excitation of O<sub>2</sub> is not important since it cannot radiate this energy. This means that vibrational excitation of CO is the only channel left for important internal excitation. Shock tube measurements yield a rate coefficient of  $2 \times 10^{-11} \text{ cm}^3 \text{ molecule}^{-1} \text{ s}^{-1}$  (Baber and Dean<sup>(26)</sup>). We have again adjusted this rate coefficient to take into account the activation energy.

Table 4 presents a summary of the rate coefficients used in these calculations and thermochemical data for the individual reactions. Figures 23-26 show the results for reaction (6a) (with vibrationally excited OH as a product), which can be compared with Figures 27-30 showing the results of reaction (7). Note that in these figures the scale was changed between the two reactions to reflect the lesser emission resulting from reaction (7). This can be seen more easily in Figure 31, for the single case of 200 km altitude and 0° angle of attack. The lesser amount of H<sub>2</sub> in the plume and the higher activation energy make the mechanism of reaction (7) generally less effective. The exception to this rule is when wide angle areas are considered and H<sub>2</sub> may be much more effective at arriving at the location prior to excitation.

Figures 32-35 show the total OH emission resulting from reactions (6a) and (7), which can be compared with the result of the generally dominant H<sub>2</sub>O mechanism in Figures 23-26. The scales are the same in these two sets of figures, and it can be seen that the total OH emission curves show

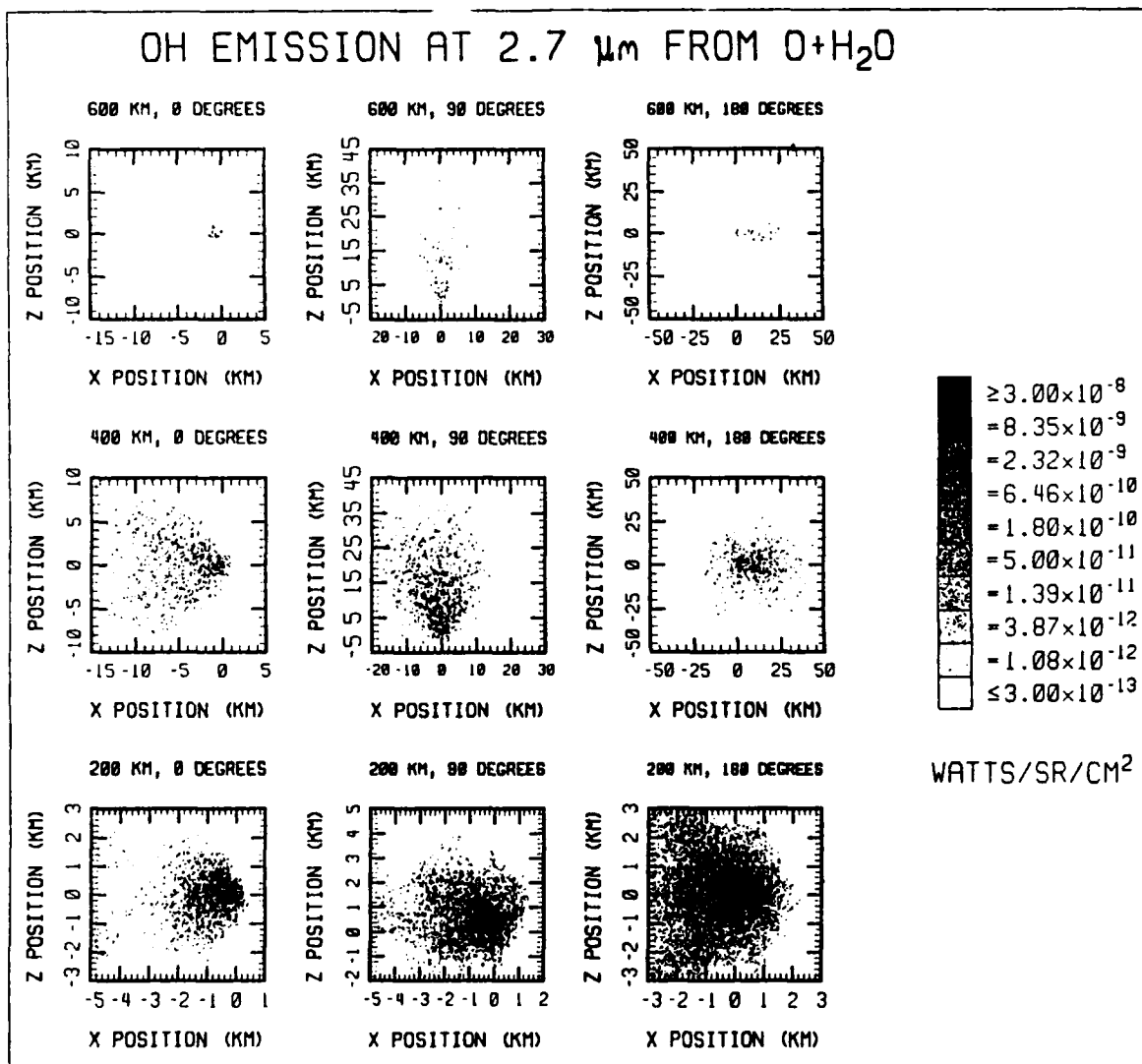


**Figure 23. A panel of gray scale plots showing the OH vibrational emission at 2.7  $\mu\text{m}$  as a result of the reaction of  $\text{O} + \text{H}_2\text{O} \rightarrow \text{OH}^* + \text{OH}$ .**

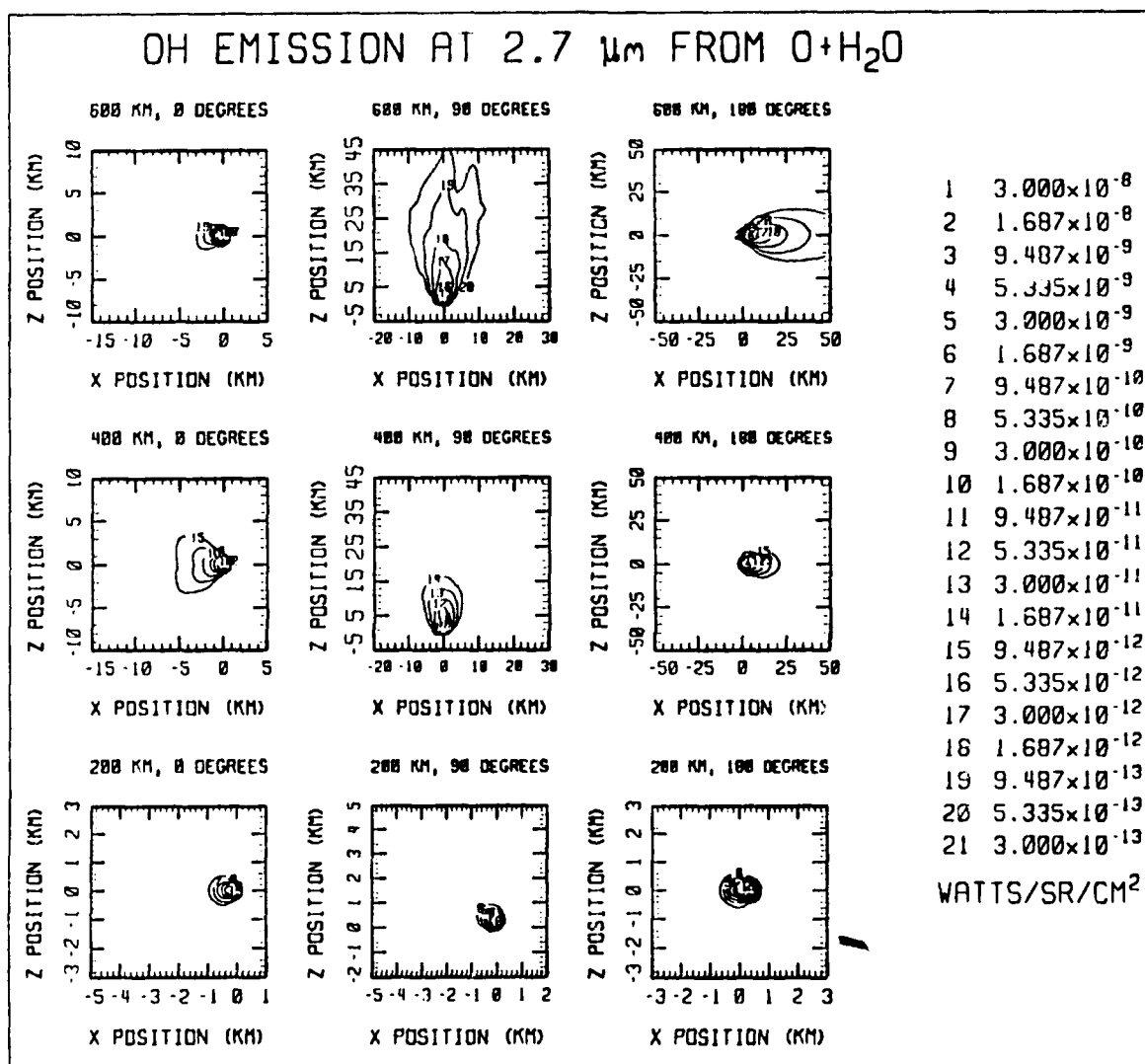
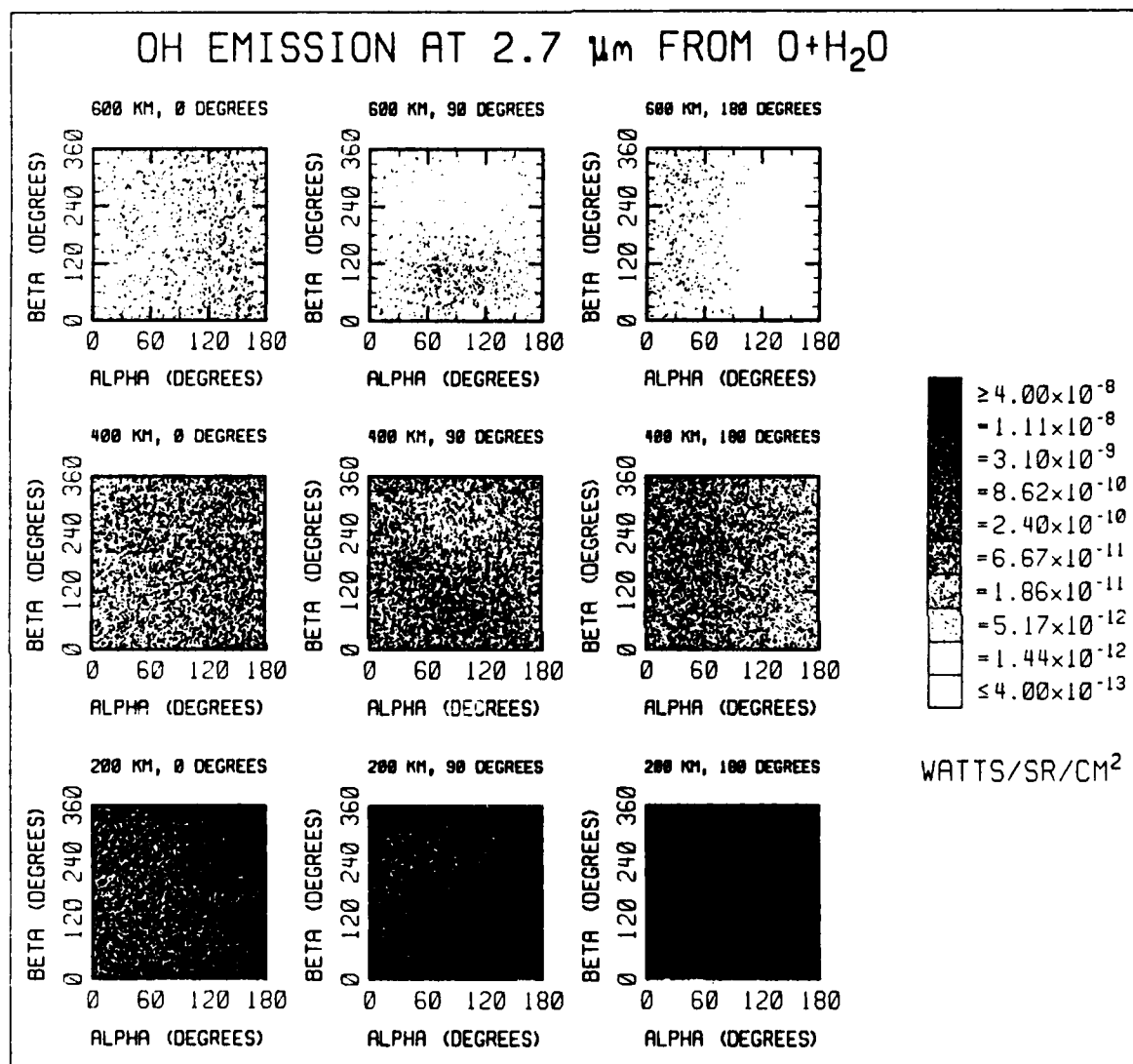


Figure 24. A panel of contour plots showing the OH vibrational emission at 2.7  $\mu\text{m}$  as a result of the reaction of  $\text{O} + \text{H}_2\text{O} \rightarrow \text{OH}^* + \text{OH}$ .



**Figure 25. A panel of gray scale plots showing the OH vibrational emission at 2.7  $\mu\text{m}$  as a result of the reaction of  $\text{O} + \text{H}_2\text{O} \rightarrow \text{OH}^* + \text{OH}$ . The emission is shown as a function of look angles for different viewing directions from the shuttle bay.**

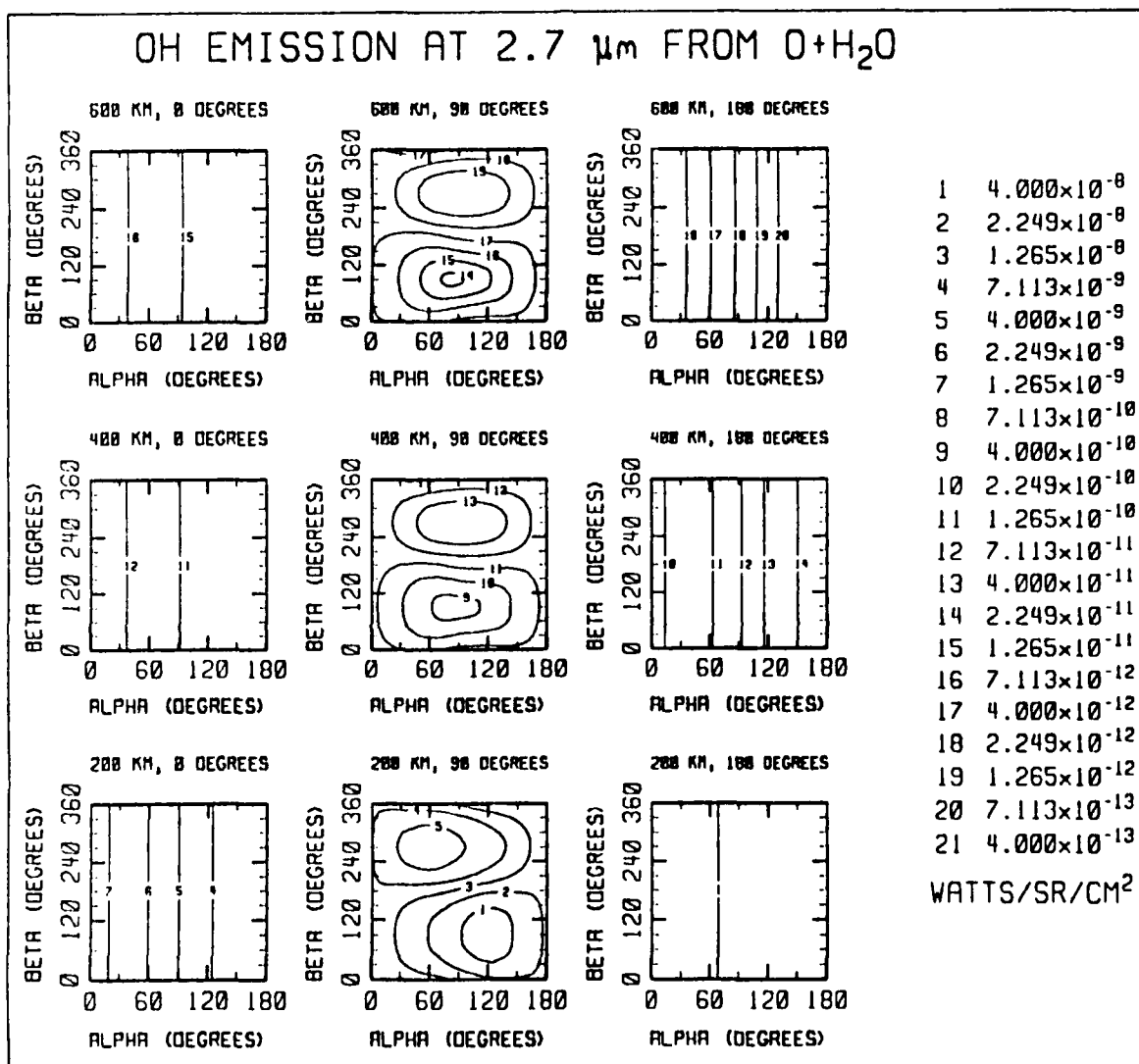


Figure 26. A panel of contour plots showing the OH vibrational emission at 2.7  $\mu\text{m}$  as a result of the reaction of  $\text{O} + \text{H}_2\text{O} \rightarrow \text{OH}^* + \text{OH}$ . The emission is shown as a function of look angles for different viewing directions from the shuttle bay.

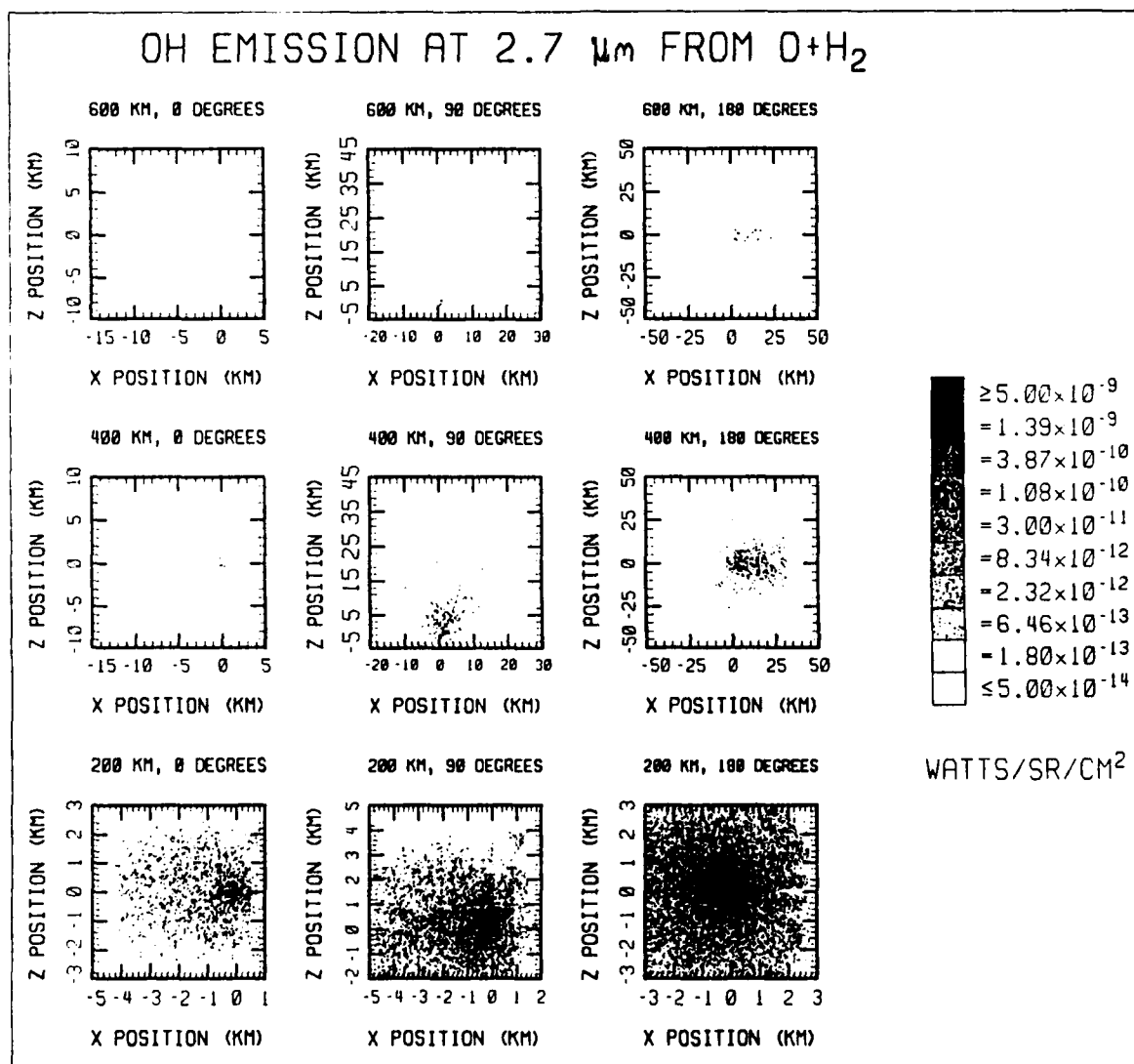


Figure 27. A panel of gray scale plots showing the OH vibrational emission at 2.7  $\mu\text{m}$  as a result of the reaction of  $\text{O} + \text{H}_2 \rightarrow \text{OH}^* + \text{H}$ .



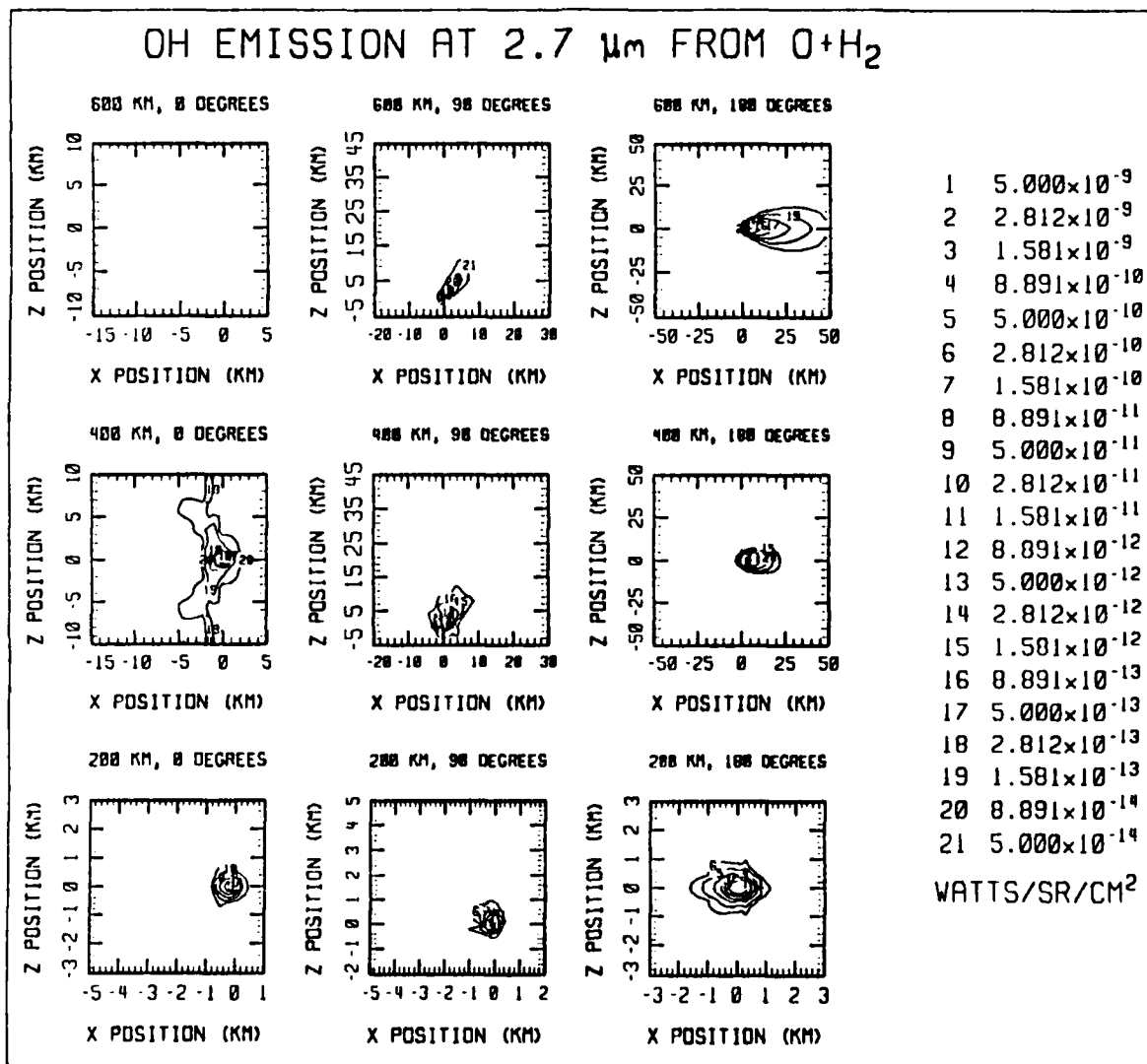


Figure 28. A panel of contour plots showing the OH vibrational emission at 2.7  $\mu\text{m}$  as a result of the reaction of  $\text{O} + \text{H}_2 \rightarrow \text{OH}^* + \text{H}$ .

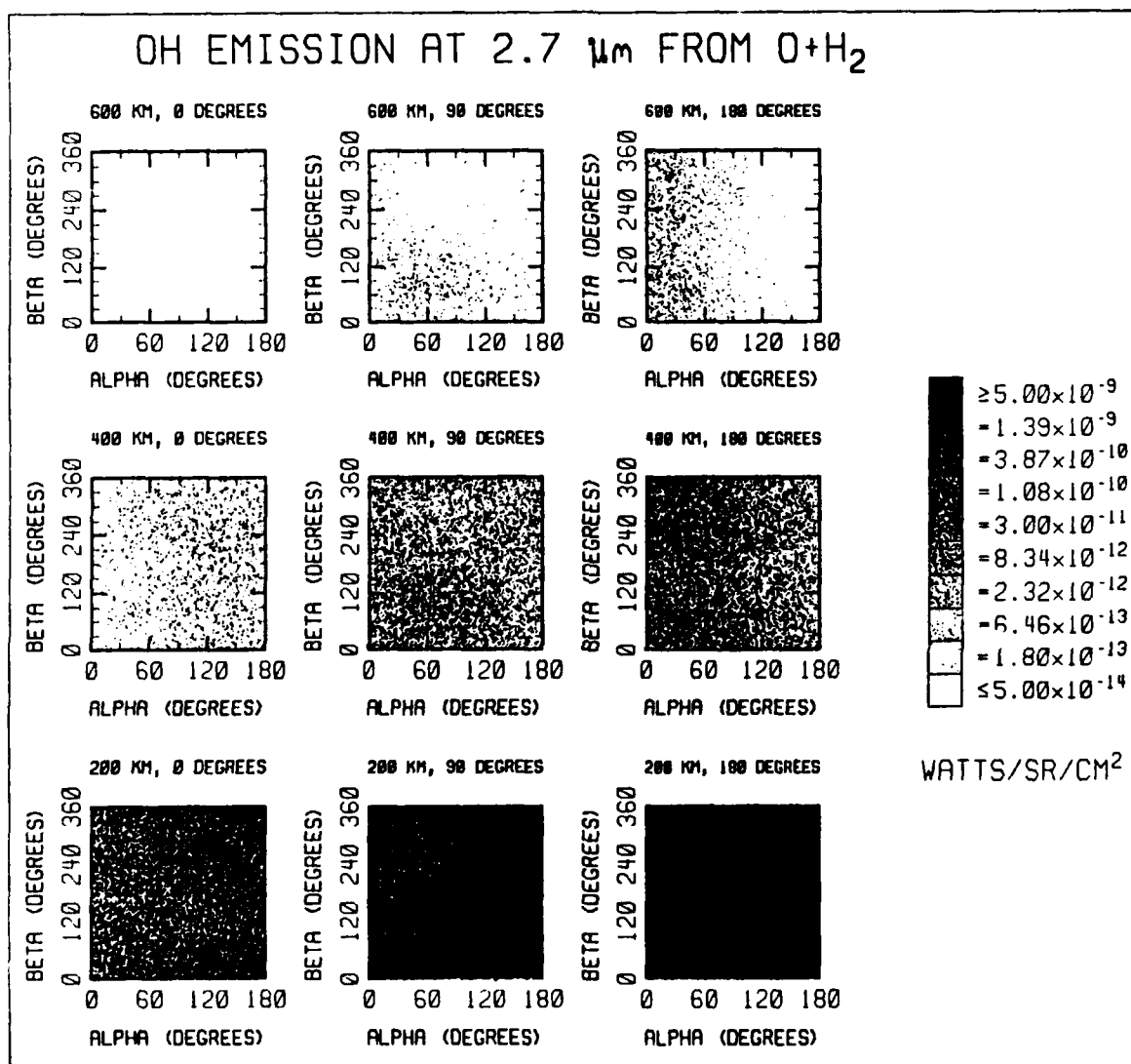


Figure 29. A panel of gray scale plots showing the OH vibrational emission at 2.7  $\mu\text{m}$  as a result of the reaction of  $\text{O} + \text{H}_2 \rightarrow \text{OH}^* + \text{H}$ . The emission is shown as a function of look angles for different viewing directions from the shuttle bay.

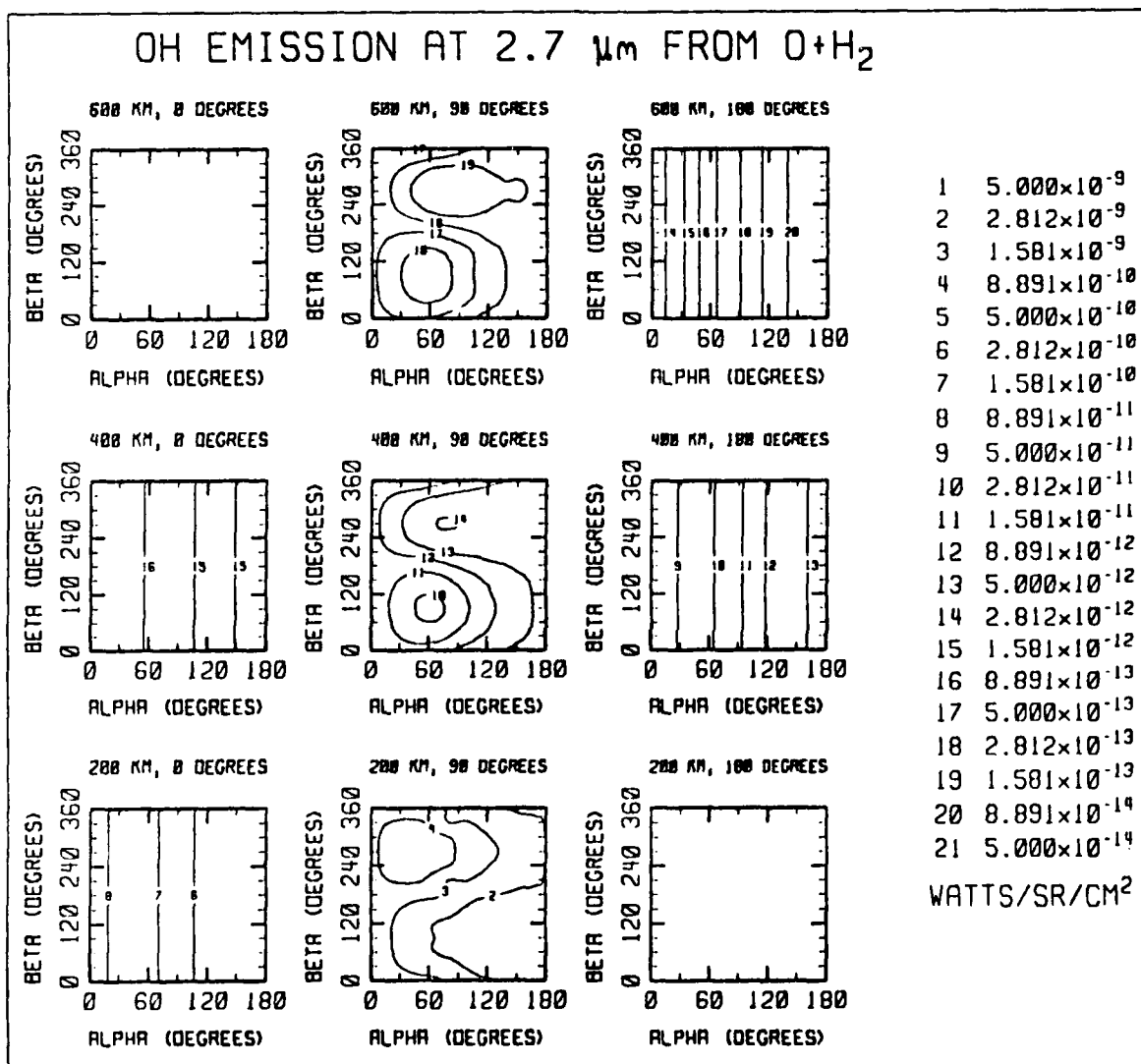


Figure 30. A panel of contour plots showing the OH vibrational emission at 2.7  $\mu\text{m}$  as a result of the reaction of  $\text{O} + \text{H}_2 \rightarrow \text{OH}^* + \text{H}$ . The emission is shown as a function of look angles for different viewing directions from the shuttle bay.

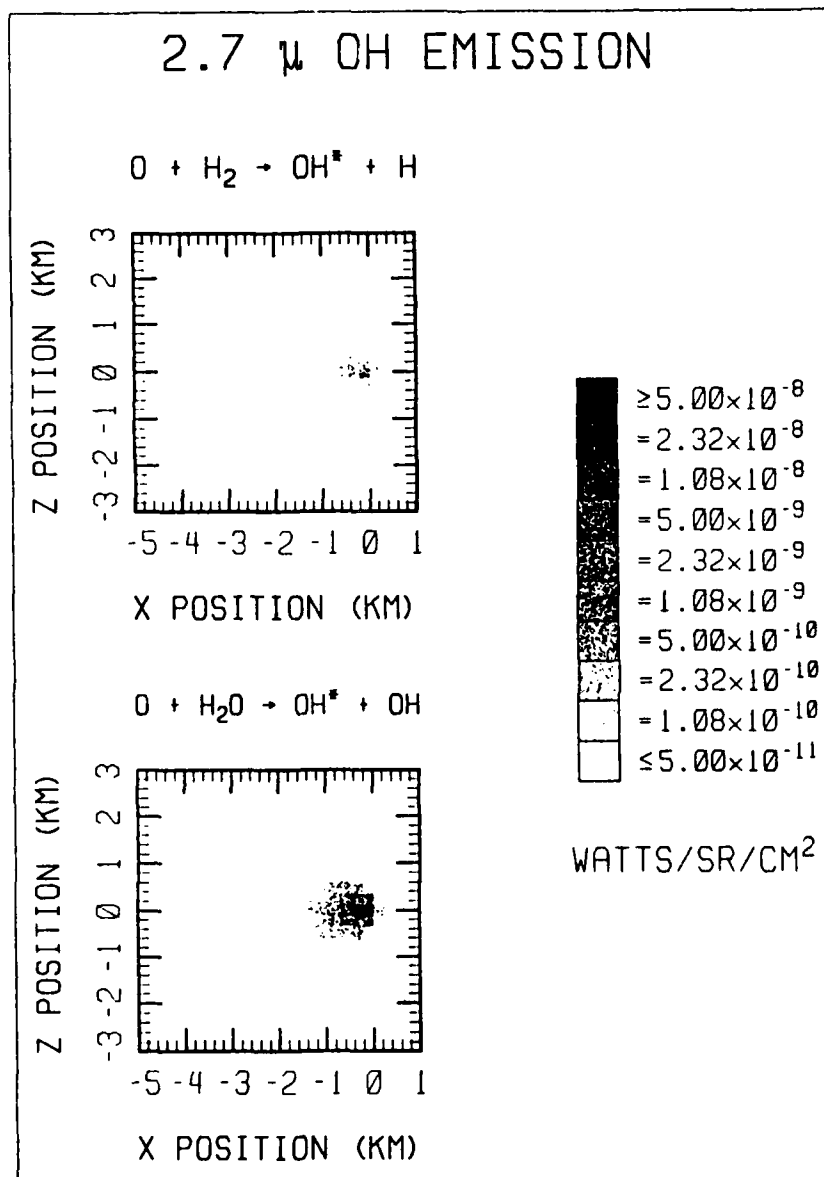


Figure 31. A comparison of OH vibrational emission at 2.7  $\mu$  for the mechanisms of  $O + H_2O$  and  $O + H_2$ . The comparison is made for 200 km and 0° angle of attack.

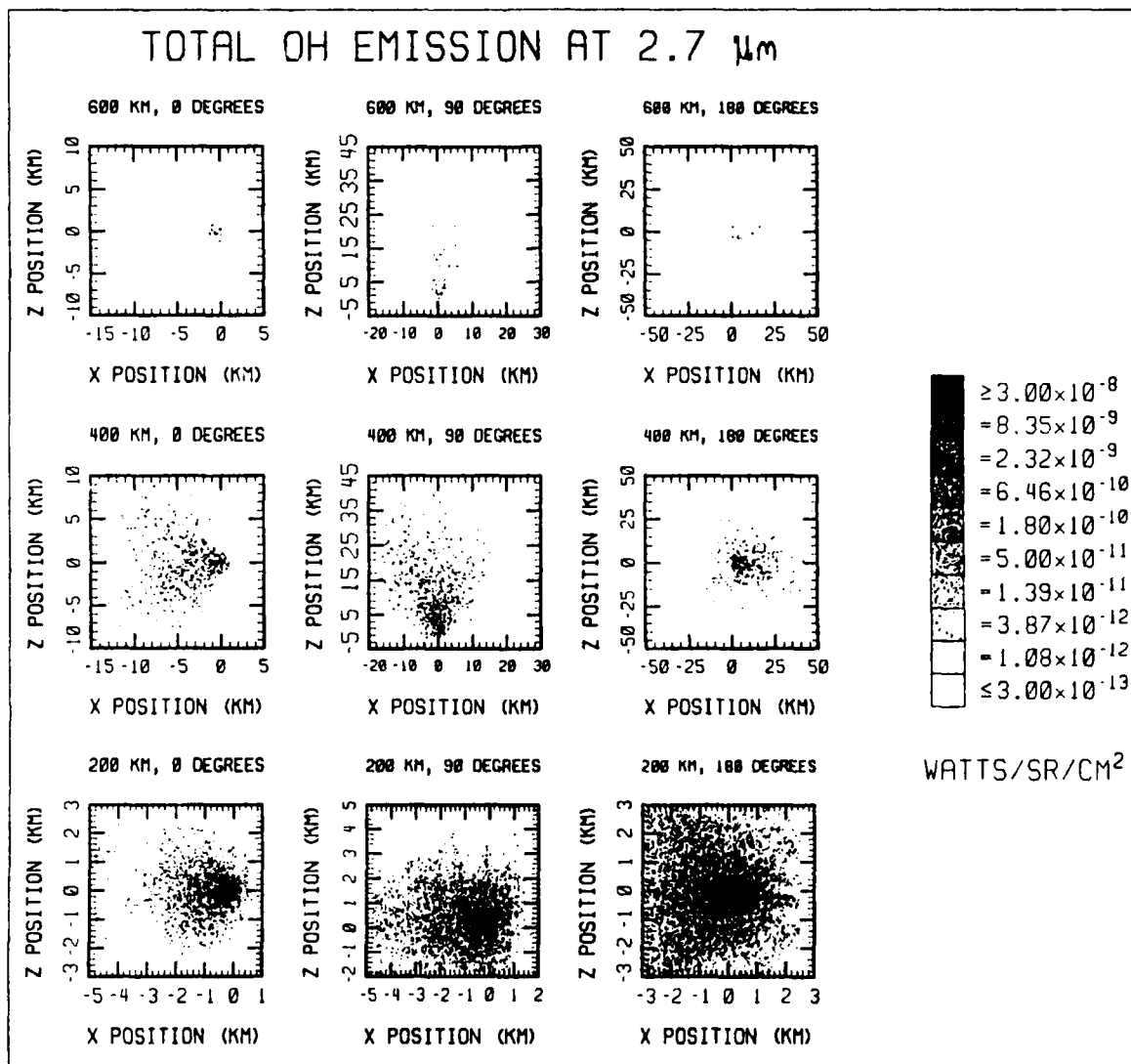


Figure 32. A panel of gray scale plots showing the total OH vibrational emission at 2.7  $\mu\text{m}$  as a result of the reactions  $\text{O} + \text{H}_2\text{O} \rightarrow \text{OH}^* + \text{OH}$  and  $\text{O} + \text{H}_2 \rightarrow \text{OH}^* + \text{H}$ .

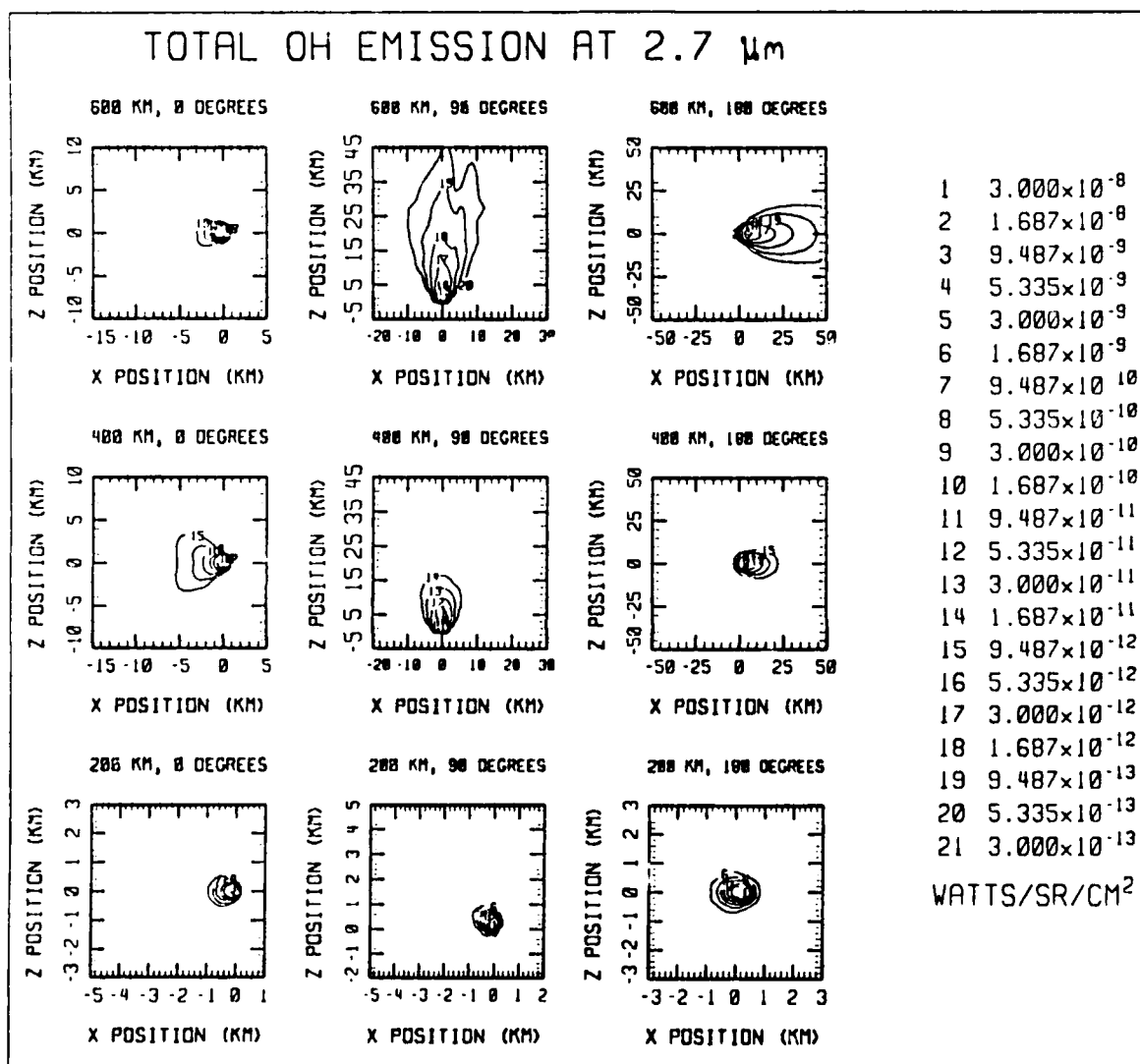


Figure 33. A panel of contour plots showing the total OH vibrational emission at 2.7  $\mu\text{m}$  as a result of the reactions  $\text{O} + \text{H}_2\text{O} \rightarrow \text{OH}^* + \text{OH}$  and  $\text{O} + \text{H}_2 \rightarrow \text{OH}^* + \text{H}$ .

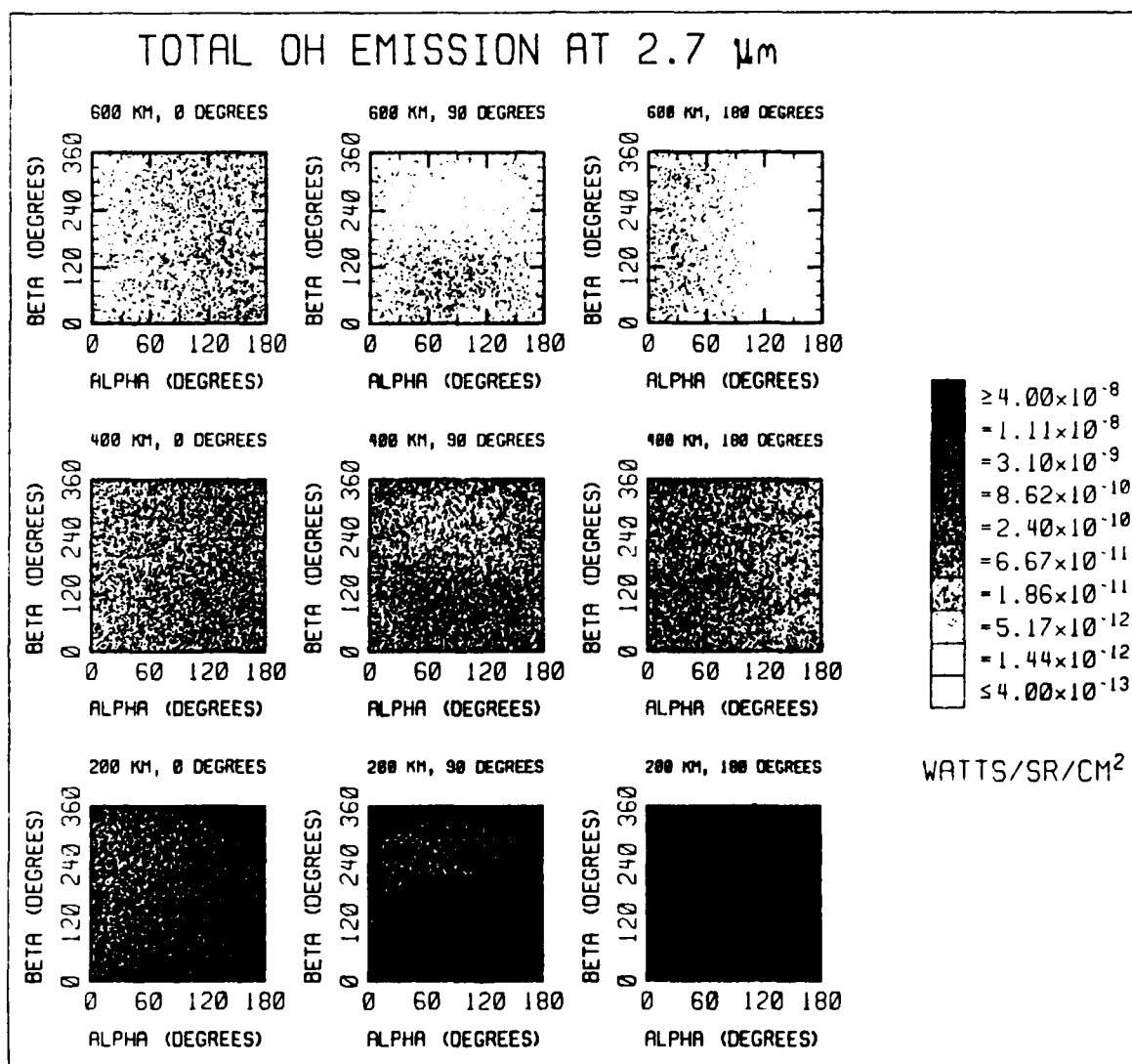


Figure 34. A panel of gray scale plots showing the total OH vibrational emission at 2.7  $\mu\text{m}$  as a result of the reactions  $\text{O} + \text{H}_2\text{O} \rightarrow \text{OH}^* + \text{OH}$  and  $\text{O} + \text{H}_2 \rightarrow \text{OH}^* + \text{H}$ . The emission is shown as a function of look angles for different viewing directions from the shuttle bay.

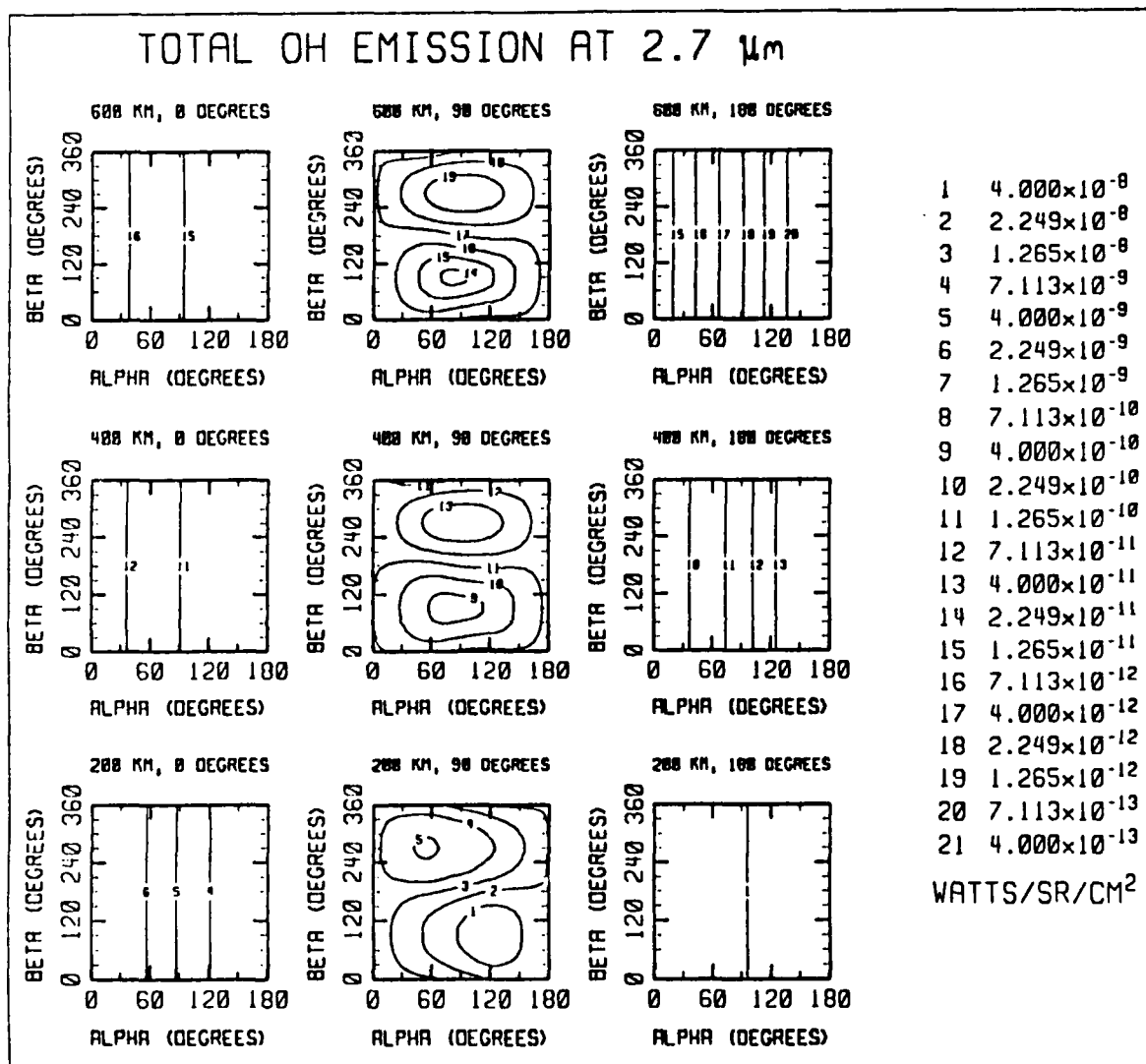


Figure 35. A panel of contour plots showing the total OH vibrational emission at 2.7  $\mu\text{m}$  as a result of the reactions  $\text{O} + \text{H}_2\text{O} \rightarrow \text{OH}^* + \text{OH}$  and  $\text{O} + \text{H}_2 \rightarrow \text{OH}^* + \text{H}$ . The emission is shown as a function of look angles for different viewing directions from the shuttle bay.



filled in regions at wide angles which are not present for the H<sub>2</sub>O mechanism alone. The difference between the two curves is the H<sub>2</sub> mechanism which, due to the greatly enhanced diffusivity of H<sub>2</sub>, shows up at the wide angles.

In comparing Figures 15-18 with Figures 32-35, it can be seen that comparable emission is predicted for the reactive mechanisms (Reactions 6a and 7) and T-V mechanism (Reaction 2). This suggests that the reactive mechanism should be considered in future 2.7 $\mu$  emission calculations.

The predicted ultraviolet emission from reaction (6b) (with electronically excited OH as a product) is shown in Figures 36-39 for all cases. The very high activation energy for this mechanism results in an emission profile which is quite different from previous density and emission profiles. In particular, the 200 km 0° case only has contributions from the very small portion of the flow which is predicted to turn and head back upstream. The model was not designed to be accurate for that portion of the flow, so such results should be considered preliminary.

The predicted CO vibrational emission from reaction (8) is shown in Figures 40-43 for all cases. In comparing these results to the direct CO<sub>2</sub> excitation shown in Figures 19-22, it is once again seen that the signatures are generally predicted to be comparable, although in this case the wavelength is shifted slightly for the CO vibrational emission.

TABLE 4  
Rate Coefficients Used in SOCRATES  
 $k = AT^n \exp(-E_a/kT)$

REACTION	A	n	E <sub>a</sub> (kcal/mole)	$\Delta H$ (kcal/mole)
2. O + H <sub>2</sub> O → O + H <sub>2</sub> O( $\nu_3$ )	1.2(-16)	1.34	10.73	10.73
3. O + CO <sub>2</sub> → O + CO <sub>2</sub> ( $\nu_3$ )	3.5(-21)	2.18	6.74	6.74
6a. O + H <sub>2</sub> O → OH + OH( $\nu=1$ )	6.6(-11)	0.00	28.00	28.0
6b. O + H <sub>2</sub> O → OH + OH(A <sup>2</sup> $\Sigma^+$ )	6.6(-11)	0.00	110.20	109.7
7. O + H <sub>2</sub> → H + OH( $\nu=1$ )	3.0(-14)	1.00	19.60	12.6
8. O + CO <sub>2</sub> → O <sub>2</sub> + CO( $\nu=1$ )	2.0(-11)	0.00	14.30	14.3

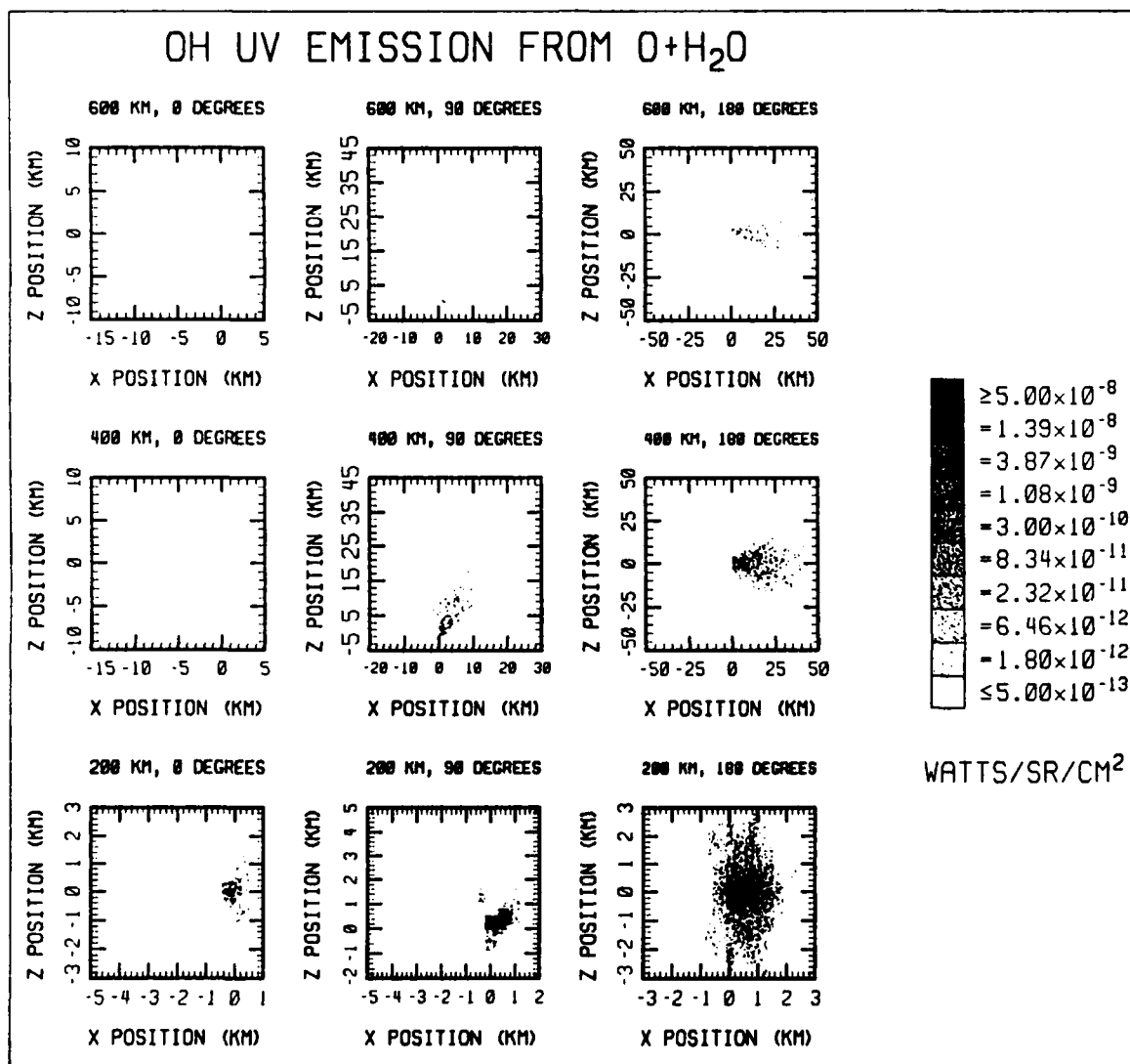


Figure 36. A panel of gray scale plots showing the OH ultraviolet emission at 306.4 nm as a result of the reaction  $O + H_2O \rightarrow OH(A) + OH$ .

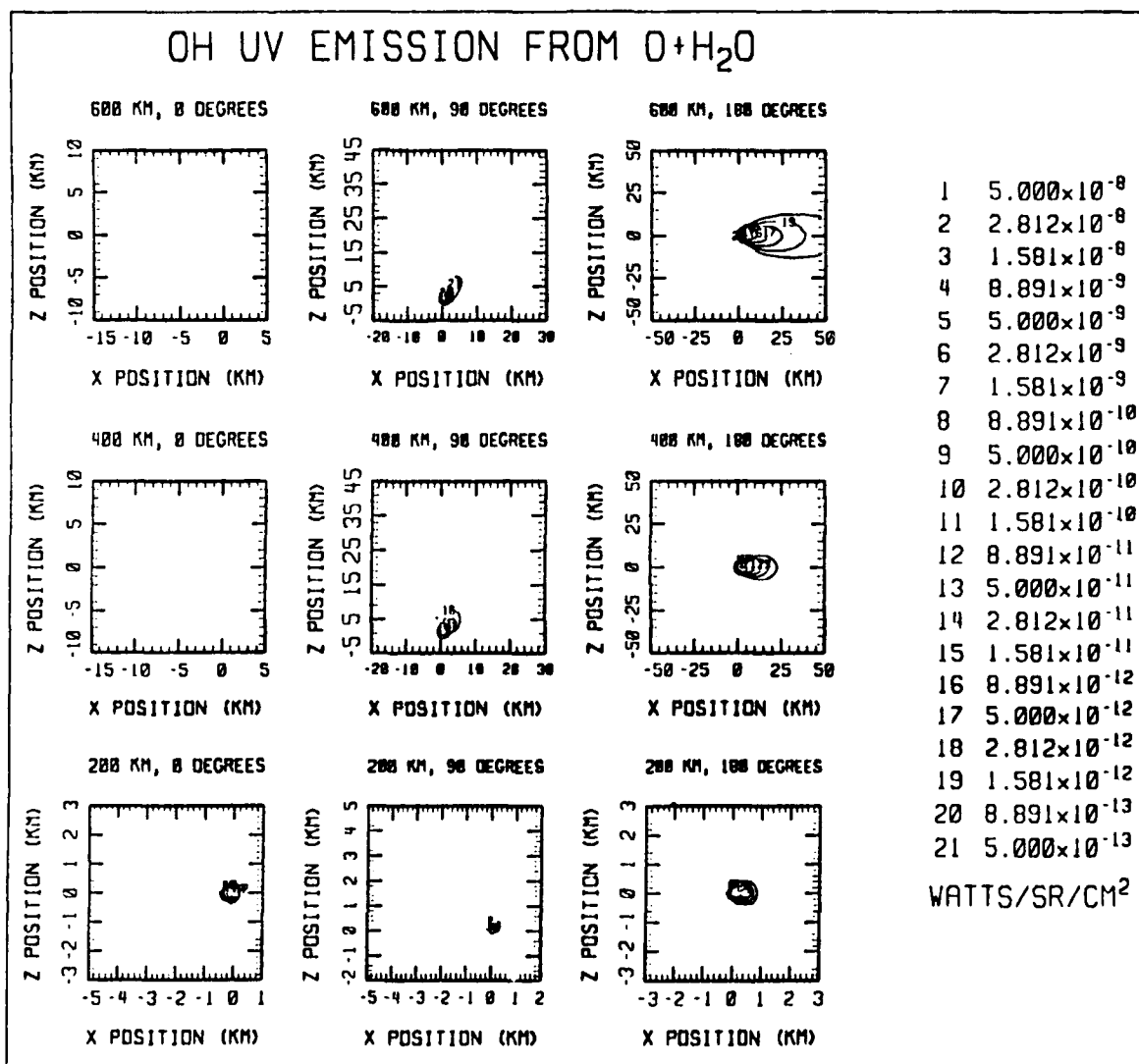


Figure 37. A panel of contour plots showing the OH ultraviolet emission at 306.4 nm as a result of the reaction  $O + H_2O \rightarrow OH(A) + OH$ .

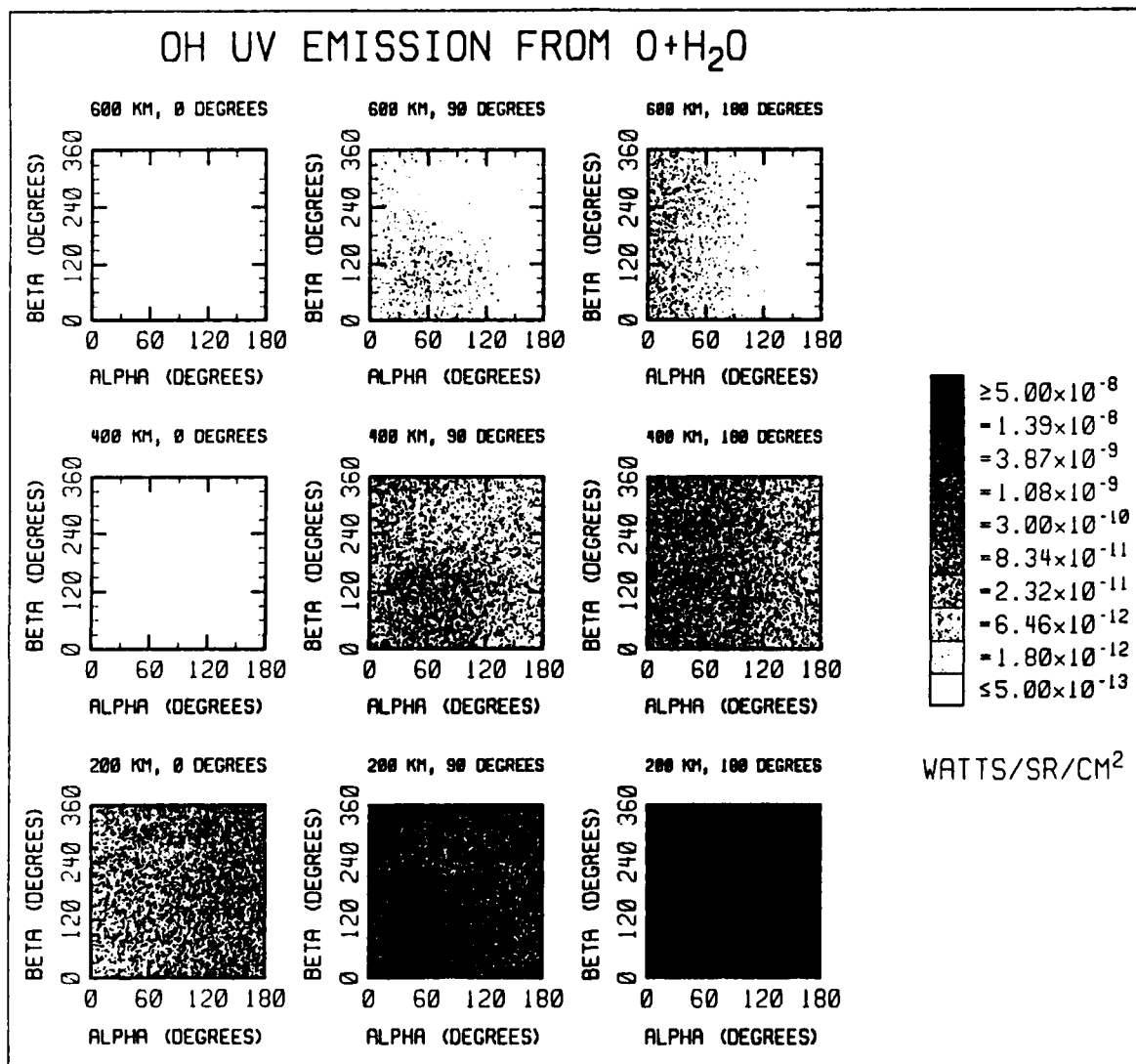


Figure 38. A panel of gray scale plots showing the OH ultraviolet emission at 306.4 nm as a result of the reaction  $O + H_2O \rightarrow OH(A) + OH$ . The emission is shown as a function of look angles for different viewing directions from the shuttle bay.

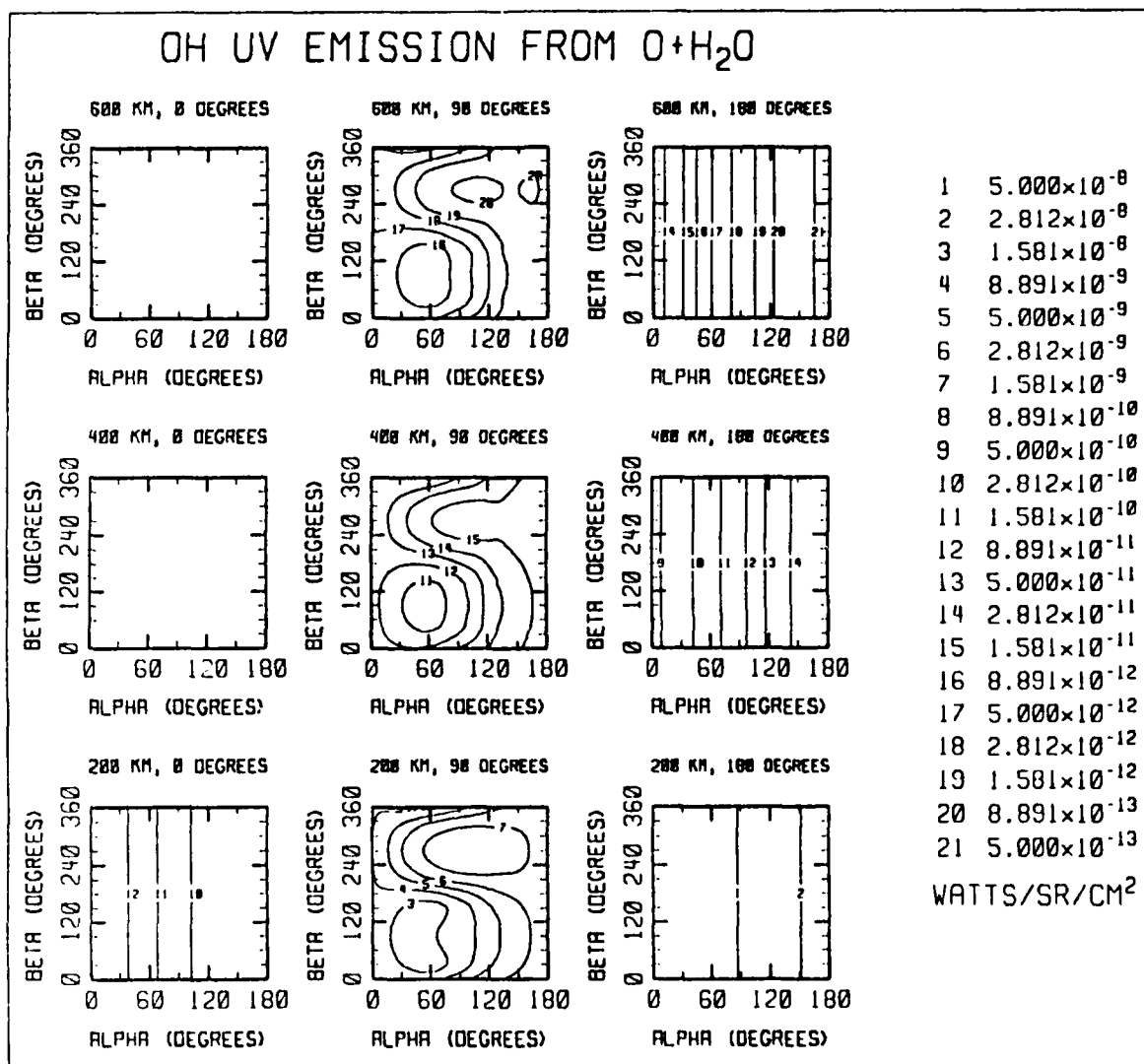
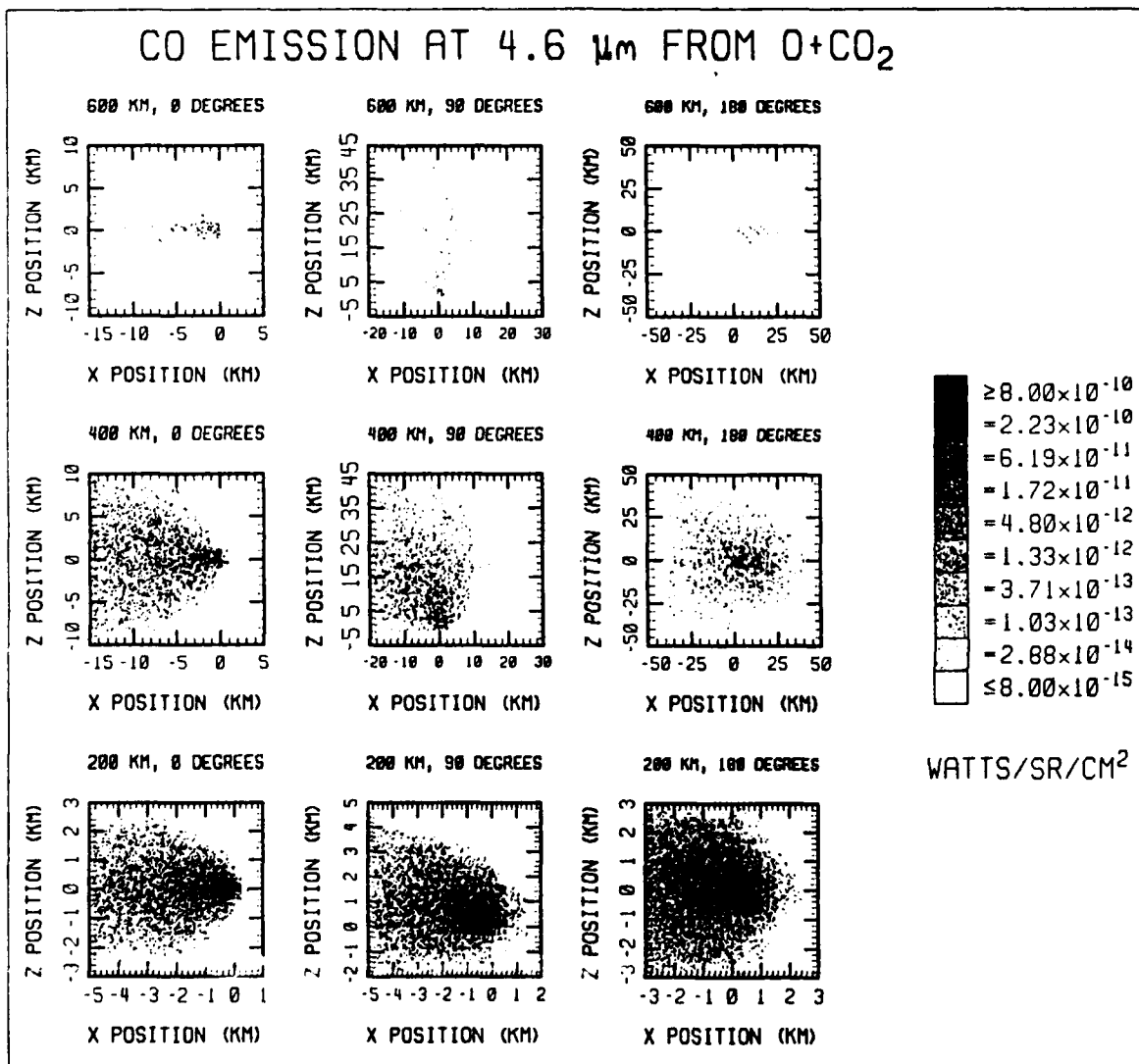
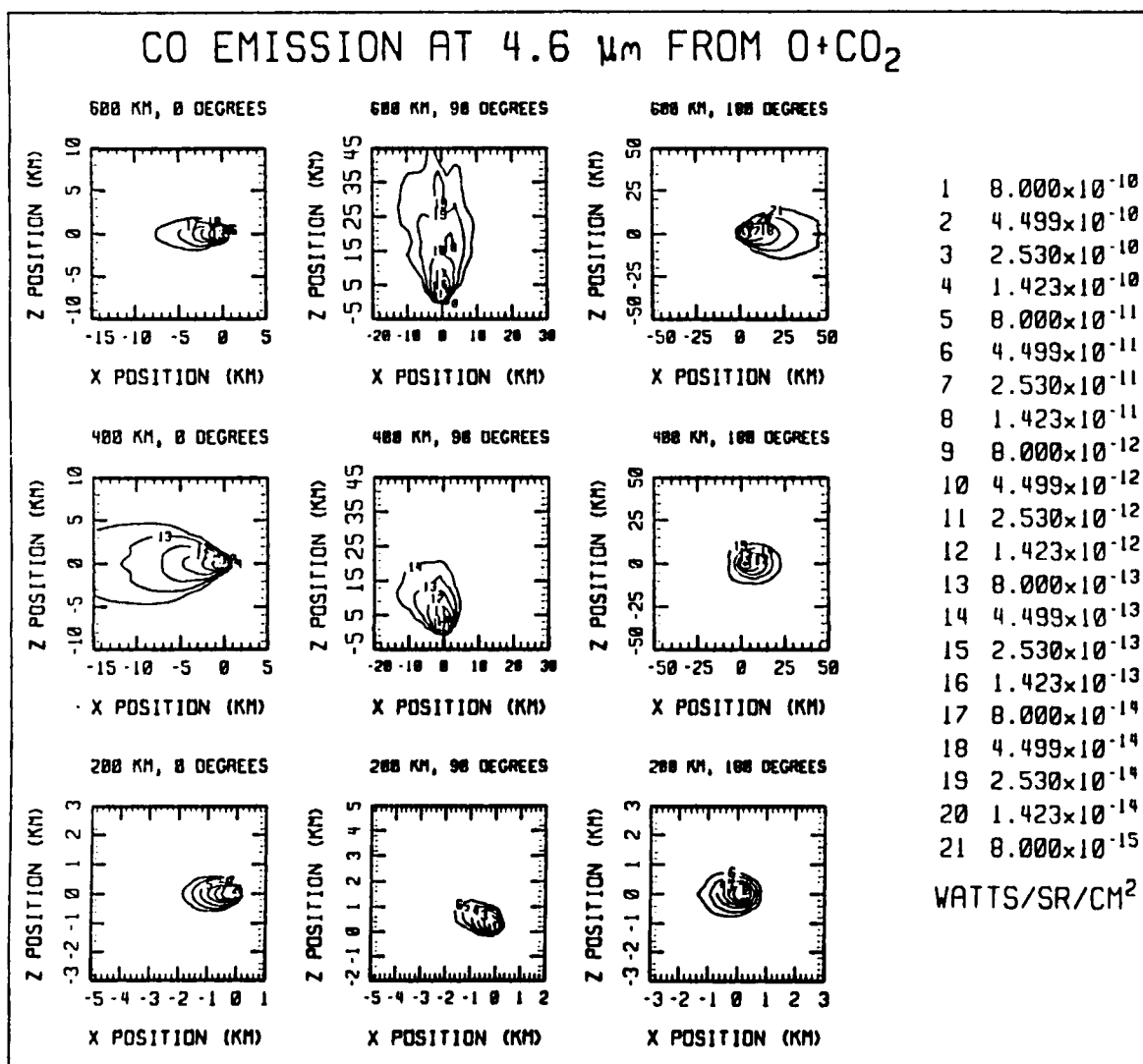


Figure 39. A panel of contour plots showing the OH ultraviolet emission at 306.4 nm as a result of the reaction  $O + H_2O \rightarrow OH(A) + OH$ . The emission is shown as a function of look angles for different viewing directions from the shuttle bay.



**Figure 40. A panel of gray scale plots showing the CO vibrational emission at 4.6  $\mu\text{m}$  as a result of the reaction of  $\text{O} + \text{CO}_2 \rightarrow \text{CO}^* + \text{O}_2$ .**



**Figure 41. A panel of contour plots showing the CO vibrational emission at 4.6  $\mu\text{m}$  as a result of the reaction of  $\text{O} + \text{CO}_2 \rightarrow \text{CO}^* + \text{O}_2$ .**

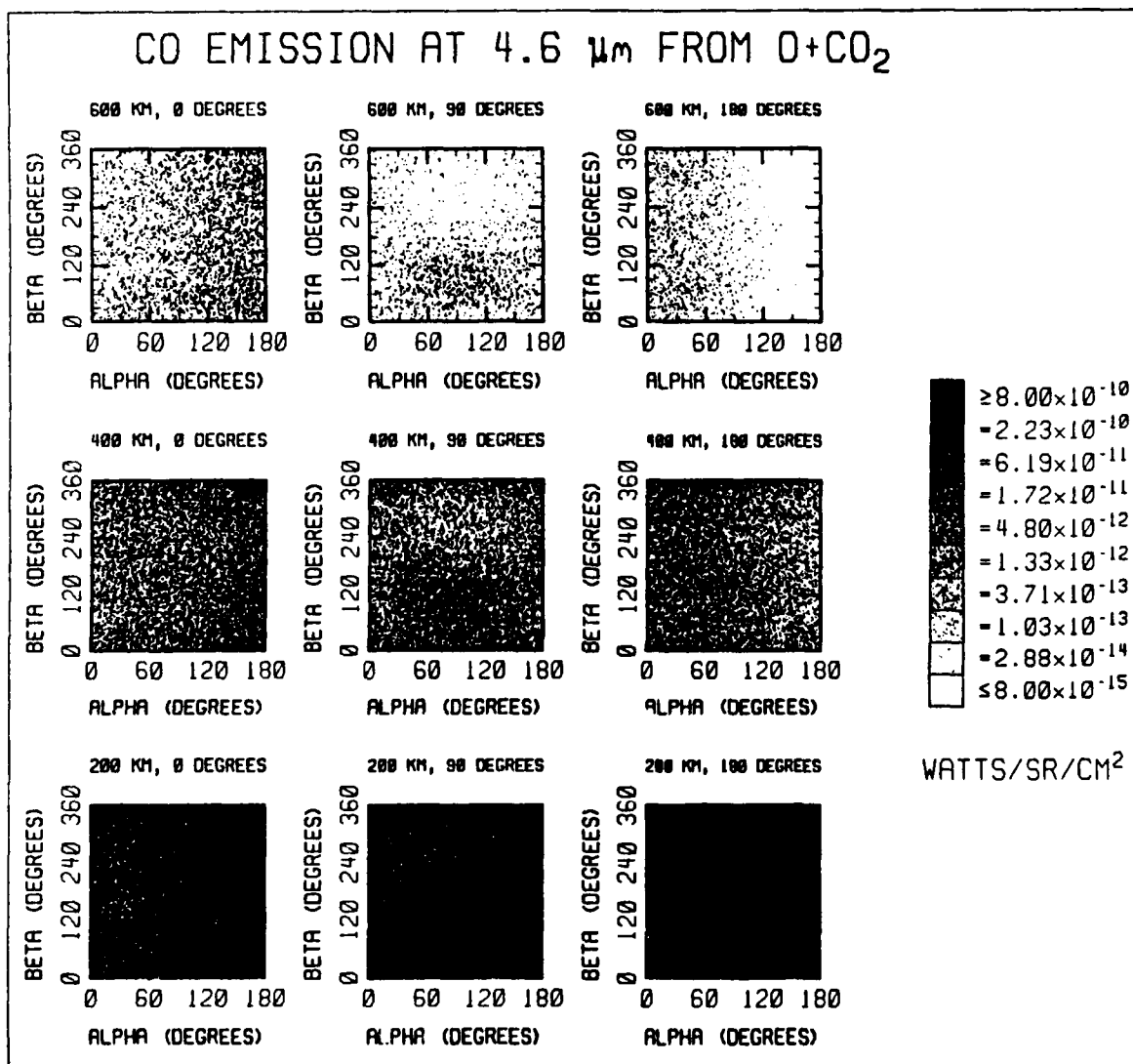


Figure 42. A panel of gray scale plots showing the CO vibrational emission at 4.6  $\mu\text{m}$  as a result of the reaction of  $\text{O} + \text{CO}_2 \rightarrow \text{CO}^* + \text{O}_2$ . The emission is shown as a function of look angles for different viewing directions from the shuttle bay.



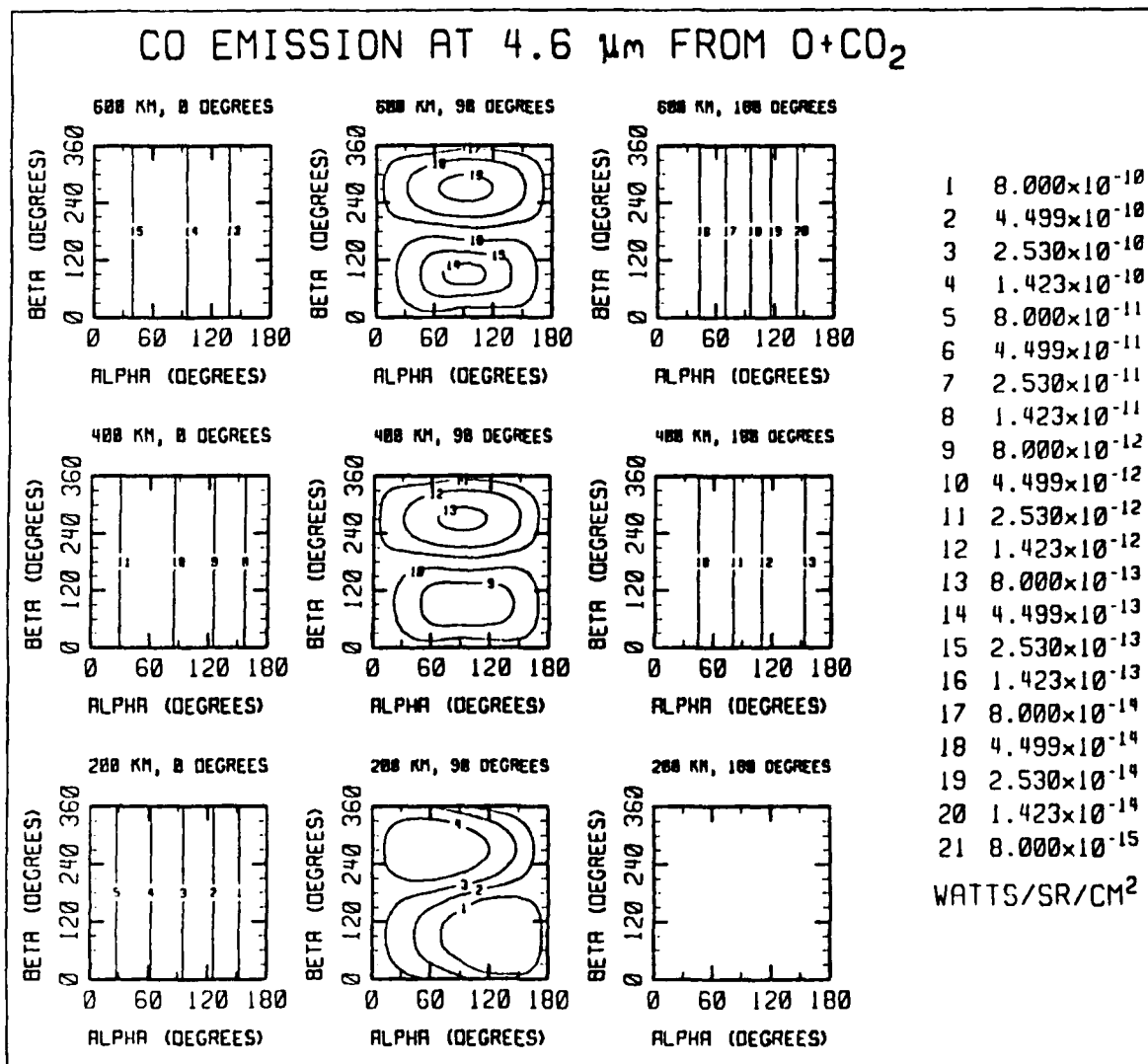


Figure 43. A panel of contour plots showing the CO vibrational emission at 4.6  $\mu\text{m}$  as a result of the reaction of  $\text{O} + \text{CO}_2 \rightarrow \text{CO}^* + \text{O}_2$ . The emission is shown as a function of look angles for different viewing directions from the shuttle bay.

## 6. SUMMARY

SOCRATES is already an effective tool, which will become even more so as the planned additional capabilities are added. It has been used to systematically investigate the effects of altitude and angle of attack on a variety of scattering, excitation and reactive mechanisms. A major new result from this work is that reactive mechanisms are predicted to be as important as collisional excitation in producing IR radiation, and potentially important in the UV, as well. The approach outlined here makes it possible to contemplate making optical measurements from the Space Shuttle or other large space platforms and planning to identify and subtract contributions from the local environment to the observed signals. A major requirement is that some information be available about the composition of the gaseous local environment.